Chemical Non-Equilibrium Reentry Flows in Two-Dimensions – Part II

EDISSON SÁVIO DE GÓES MACIEL[(1)] AND AMILCAR PORTO PIMENTA[(2)]
IEA – Aeronautical Engineering Division
ITA – Aeronautical Technological Institute
Praça Mal. Eduardo Gomes, 50 – Vila das Acácias – São José dos Campos – SP – 12228-900
BRAZIL
edisavio@edissonsavio.eng.br[(1)], http://www.edissonsavio.eng.br[(1)] and amilcar@ita.br[(2)]

Abstract: - This work, second part of this study, presents two numerical tools implemented to simulate inviscid and viscous flows employing the reactive gas formulation of thermal equilibrium and chemical non-equilibrium. The Euler and Navier-Stokes equations, employing a finite volume formulation, on the context of structured and unstructured spatial discretizations, are solved. The aerospace problems involving the hypersonic flow around a blunt body, around a double ellipse, and around a re-entry capsule, in two-dimensions, are simulated. The reactive simulations will involve an air chemical model of five species: N, N_2, NO, O and O_2. Seventeen chemical reactions, involving dissociation and recombination, will be simulated by the proposed model. The algorithms employed to solve the reactive equations were the Van Leer and the Liou and Steffen Jr., first- and second-order accurate ones. The second-order numerical scheme is obtained by a "MUSCL" (Monotone Upstream-centered Schemes for Conservation Laws) extrapolation process in the structured case. The algorithms are accelerated to the steady state solution using a spatially variable time step procedure, which has demonstrated effective gains in terms of convergence rate, as reported in Maciel. The results have demonstrated that the most correct aerodynamic coefficient of lift to the re-entry problem is obtained by the Van Leer first-order accurate scheme in the viscous, structured simulation. The Van Leer scheme is also the most robust being able to simulate the major part of the studied problems.

Key-Words: - Euler and Navier-Stokes equations, Chemical non-equilibrium, Five species model, Hypersonic flow, Van Leer algorithm, Liou and Steffen Jr. algorithm.

1 Introduction

In several aerodynamic applications, the atmospheric air, even being composed of several chemical species, can be considered as a perfect thermal and caloric gas due to its inert property as well its uniform composition in space and constancy in time. However, there are several practical situations involving chemical reactions, as for example: combustion processes, flows around aerospace vehicles in re-entry conditions or plasma flows, which do not permit the ideal gas hypothesis ([1]). As described in [2], since these chemical reactions are very fast such that all processes can be considered in equilibrium, the conservation laws which govern the fluid become essentially unaltered, except that one equation to the general state of equilibrium has to be used opposed to the ideal gas law. When the flow is not in chemical equilibrium, one mass conservation law has to be written to each chemical species and the size of the equation system increases drastically.

To the motivation of the present work and to the theoretical background to understand this one, the reader is encouraged to read the first part of this study [3]. This paper complements the present work and finishes such study.

This work, second part of this study, presents two numerical tools implemented to simulate inviscid and viscous flows employing the reactive gas formulation of thermal equilibrium and chemical non-equilibrium flow in two-dimensions. The Euler and Navier-Stokes equations, employing a finite volume formulation, on the context of structured and unstructured spatial discretizations, are solved. These variants allow an effective comparison between the two types of spatial discretization aiming verify their potentialities: solution quality, convergence speed, computational cost, etc. The aerospace problems involving the "hot gas" hypersonic flow around a blunt body, around a double ellipse, and around a re-entry capsule in two-dimensions, are simulated. The algorithms are accelerated to the steady state solution using a spatially variable time step procedure, which has demonstrated effective gains in terms of convergence rate, as shown in [4-5].

The reactive simulations will involve an air chemical model of five species: N, O, N_2, O_2 and NO. Seventeen chemical reactions, involving dissociation and recombination, will be simulated

by the proposed model. The Arrhenius formula will be employed to determine the reaction rates and the law of mass action will be used to determine the source terms of each gas species equation.

The algorithms employed to solve the reactive equations were the [6-7], first- and second-order accurate ones. The second-order numerical scheme is obtained by a MUSCL extrapolation process in the structured case. In the unstructured case, tests with the linear reconstruction process did not yield converged results and, therefore, were not presented. Only first-order solutions are presented. The algorithm was implemented in a FORTRAN programming language, using the software Microsoft Developer Studio. Simulations in a notebook with processor PENTIUM INTEL Duo Core 2.30 GHz of clock and 2 GBytes of RAM were performed.

The results have demonstrated that the most correct aerodynamic coefficient of lift, to the re-entry capsule, is obtained by the [6] first-order accurate scheme in the viscous and structured simulation. Moreover, the [6] scheme is also the most robust being able to simulate the major part of the studied problems

2 Unstructured Formulation and the Liou and Steffen Jr. Scheme

The Euler and Navier-Stokes equations are presented in details in [3] and because it is not presented here again. The thermodynamic and transport properties are also described in [3], as well the chemical formulation, and are not repeated herein. Only the unstructured formulation and the [7] algorithm were not presented and are detailed in this work.

2.1. Unstructured formulation

The cell volume on an unstructured context is defined by:

$$V_i = 0.5\left|\left(x_{n1}y_{n2} + y_{n1}x_{n3} + x_{n2}y_{n3}\right) - \left(x_{n3}y_{n2} + y_{n3}x_{n1} + x_{n2}y_{n1}\right)\right|, \quad (1)$$

with n_1, n_2 and n_3 being the nodes of a given triangular cell. The description of the computational cell and its nodes, flux interfaces and neighbours are shown in Fig. 1.

The area components at the "l" interface are defined by:

$$S_x^l = n_x^l S^l \quad \text{and} \quad S_y^l = n_y^l S^l, \quad (2)$$

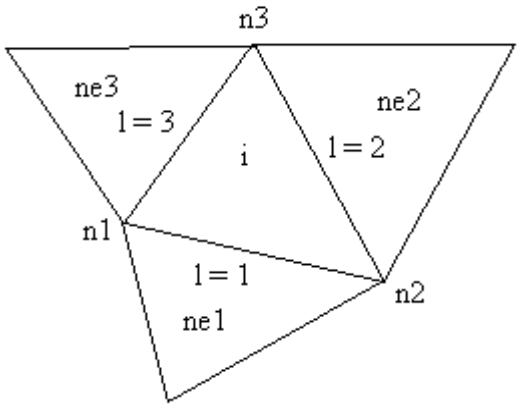

Figure 1. Unstructured computational cell.

where n_x^l, n_y^l and S^l are defined as:

$$n_x^l = \Delta y_l / \left(\Delta x_l^2 + \Delta y_l^2\right)^{0.5},$$
$$n_y^l = -\Delta x_l / \left(\Delta x_l^2 + \Delta y_l^2\right)^{0.5};$$
$$S^l = \left(\Delta x_l^2 + \Delta y_l^2\right)^{0.5}. \quad (3)$$

Expressions to Δx_l and Δy_l are given in Tab. 1.

Table 1. Values of Δx_l and Δy_l.

Interface	Δx_l	Δy_l
l = 1	$x_{n2} - x_{n1}$	$y_{n2} - y_{n1}$
l = 2	$x_{n3} - x_{n2}$	$y_{n3} - y_{n2}$
l = 3	$x_{n1} - x_{n3}$	$y_{n1} - y_{n3}$

Considering the two-dimensional and unstructured case, the algorithm follows that described in [3]. Defining R_l the residual obtained by the numerical algorithm, which is composed by the inviscid contribution minus the viscous contribution, the discrete-dynamic-convective flux is defined by:

$$R_1 = |S|_1 \left\{ \frac{1}{2} M_1 \left[\begin{pmatrix} \rho a \\ \rho a u \\ \rho a v \\ \rho a H \end{pmatrix}_L + \begin{pmatrix} \rho a \\ \rho a u \\ \rho a v \\ \rho a H \end{pmatrix}_R \right] - \frac{1}{2} \phi_1 \left[\begin{pmatrix} \rho a \\ \rho a u \\ \rho a v \\ \rho a H \end{pmatrix}_R - \begin{pmatrix} \rho a \\ \rho a u \\ \rho a v \\ \rho a H \end{pmatrix}_L \right] \right\} + \begin{pmatrix} 0 \\ S_x p \\ S_y p \\ 0 \end{pmatrix}_1, \quad (4)$$

and the discrete-chemical-convective flux is defined by:

$$R_1 = |S|_1 \left\{ \frac{1}{2} M_1 \left[\begin{pmatrix} \rho_1 a \\ \rho_2 a \\ \rho_4 a \\ \rho_5 a \end{pmatrix}_L + \begin{pmatrix} \rho_1 a \\ \rho_2 a \\ \rho_4 a \\ \rho_5 a \end{pmatrix}_R \right] - \frac{1}{2} \phi_1 \left[\begin{pmatrix} \rho_1 a \\ \rho_2 a \\ \rho_4 a \\ \rho_5 a \end{pmatrix}_R - \begin{pmatrix} \rho_1 a \\ \rho_2 a \\ \rho_4 a \\ \rho_5 a \end{pmatrix}_L \right] \right\}, \quad (5)$$

The time integration is performed by the Runge-Kutta explicit method of five stages, second-order accurate, to the two types of convective flux. To the dynamic part, this method can be represented in general form by:

$$\begin{aligned} Q_i^{(0)} &= Q_i^{(n)} \\ Q_i^{(k)} &= Q_i^{(0)} - \alpha_k \Delta t_i \, R\left(Q_i^{(k-1)}\right) / V_i \, , \\ Q_i^{(n+1)} &= Q_i^{(k)} \end{aligned} \quad (6)$$

and to the chemical part, it can be represented in general form by:

$$\begin{aligned} Q_i^{(0)} &= Q_i^{(n)} \\ Q_i^{(k)} &= Q_i^{(0)} - \alpha_k \Delta t_i \left[R\left(Q_i^{(k-1)}\right) / V_i - S_C\left(Q_i^{(k-1)}\right) \right], \\ Q_i^{(n+1)} &= Q_i^{(k)} \end{aligned} \quad (7)$$

where the chemical source term S_C is calculated with the translational/rotational temperature, k = 1,...,5; $\alpha_1 = 1/4$, $\alpha_2 = 1/6$, $\alpha_3 = 3/8$, $\alpha_4 = 1/2$ and $\alpha_5 = 1$.

2.2. Liou and Steffen Jr. algorithm

The appropriated choice of the ϕ_l term defines the [7] scheme according to [8]. Hence, the following definition describes the [7] scheme:

$$\phi_l = M_l \quad \text{or} \quad \phi_{i+1/2,j} = M_{i+1/2,j} \, , \quad (8)$$

for unstructured and structured cases, respectively.

The viscous formulation follows that of [9], which adopts the Green theorem to calculate primitive variable gradients. The viscous vectors are obtained by arithmetical average of flow properties between cell (i,j) and its neighbors. As was done with the convective terms, there is a need to separate the viscous flux in two parts: dynamical viscous flux and chemical viscous flux. The dynamical part corresponds to the first four equations of the Navier-Stokes ones and the chemical part corresponds to the last four equations.

A spatially variable time step procedure was employed aiming to accelerate the convergence of the numerical schemes. This technique has provided excellent convergence gains as demonstrated in [4-5] and is implemented in the present codes.

3 Results

Four (4) orders of reduction of the maximum residual were adopted as convergence criterion. In the simulations, the attack angle was set equal to zero.

3.1 Initial and boundary conditions to the studied problem

The initial conditions are presented in Table 2. The Reynolds number is obtained from data of [10]. The boundary conditions to this problem of reactive flow are detailed in [11], as well the blunt body geometry, the meshes employed in the simulations and the description of the computational configuration. As aforementioned, the first geometry is a blunt body with 1.0 m of nose ratio and parallel rectilinear walls. The far field is located at 20.0 times the nose ratio in relation to the configuration nose.

Table 2. Initial conditions to the problem of the blunt body.

Property	Value
M_∞	8.78
ρ_∞	0.00326 kg/m^3
p_∞	687.0 Pa
U_∞	4,776 m/s
T_∞	694.0 K
Altitude	40,000 m
c_N	10^{-9}
c_O	0.07955
c_{O2}	0.13400
c_{NO}	0.05090
L	2.0 m
Re_∞	2.3885x10^6

3.2. Blunt body results

3.2.1. Inviscid, unstructured and first-order accurate case – Same sense

Figures 2 and 3 present the pressure contours in the field obtained by the [6] and the [7] schemes, respectively. The [7] scheme predicts the most

severe pressure peak of approximately 159 unities. The [6] solution shows good symmetry properties. There are not pre- or post-shock oscillations.

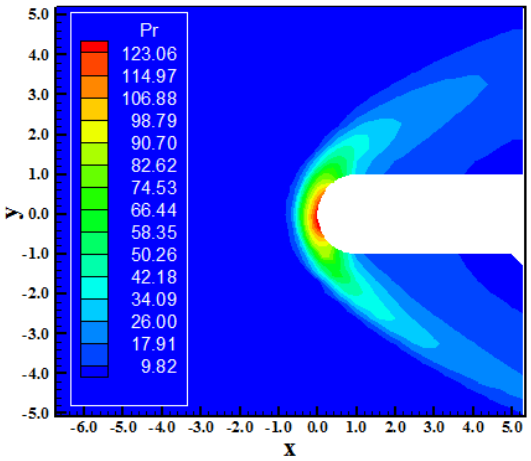

Figure 2. Pressure Contours (VL).

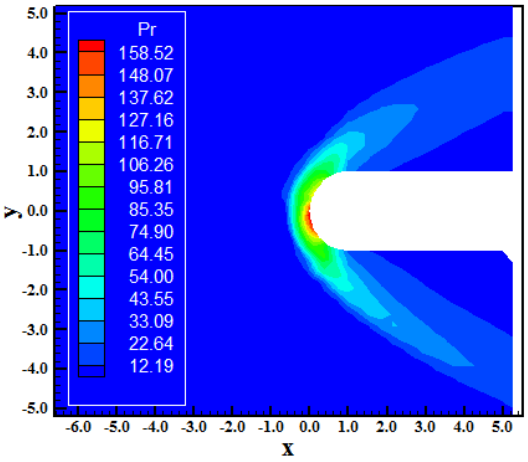

Figure 3. Pressure Contours (LS).

Figures 4 and 5 exhibit the Mach number contours generated by the [6-7] algorithms, respectively. Good symmetry properties are again observed in both solutions and the shock is well captured by both schemes. The flow is slowdown due to the presence of the configuration and in the line of stagnation, behind the shock, the flow is subsonic.

Figures 6 and 7 show the translational / rotational temperature contours obtained by the [6] and the [7] numerical algorithms. The most intense temperature field is obtained by the [6] scheme. Good symmetry properties are observed in the [6] solution. The shock wave is well captured by both algorithms.

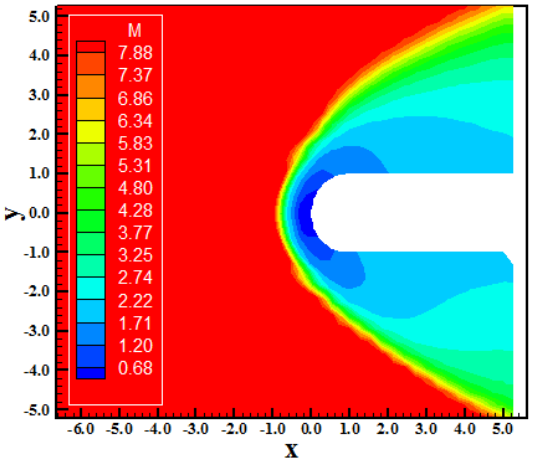

Figure 4. Mach Number Contours (VL).

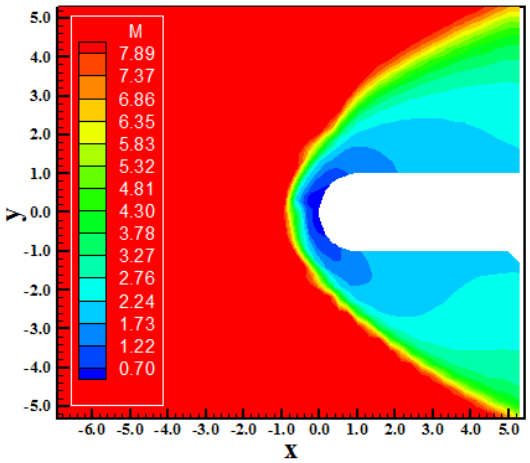

Figure 5. Mach Number Contours (LS).

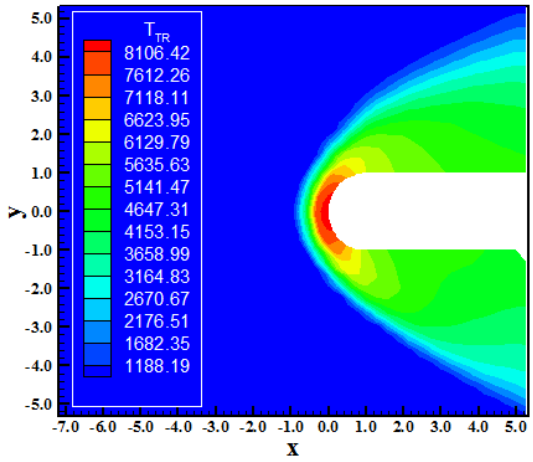

Figure 6. T/R Temperature Contours (VL).

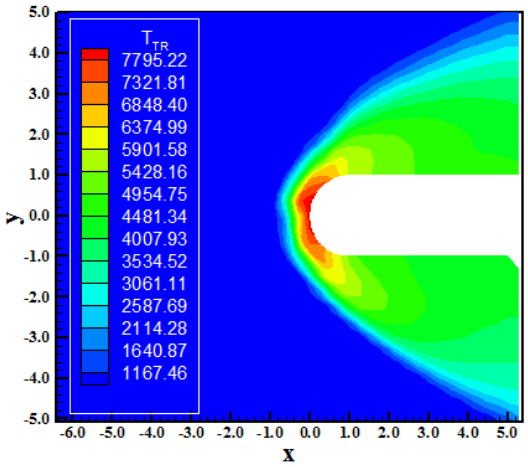

Figure 7. T/R Temperature Contours (LS).

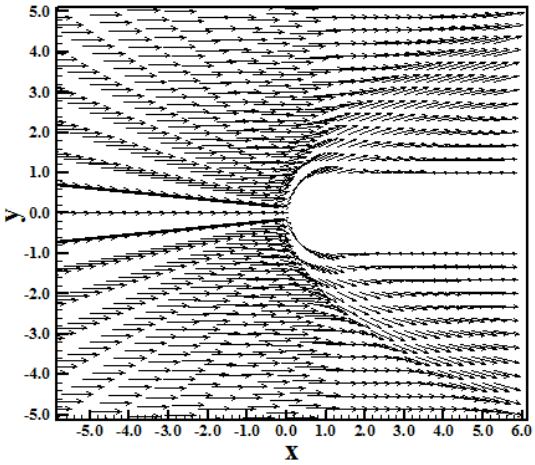

Figure 8. Velocity Vector Field (VL).

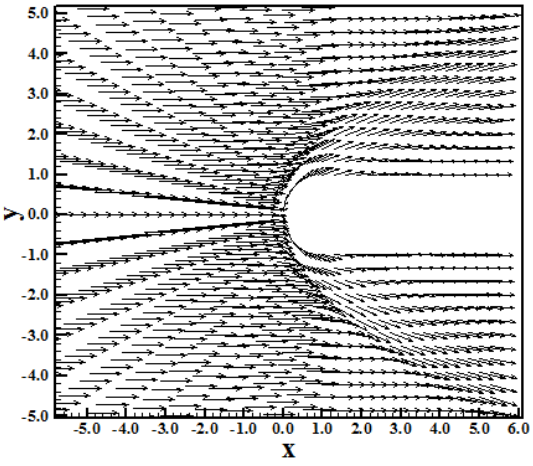

Figure 9. Velocity Vector Field (LS).

Figure 8 and 9 present the flow velocity vector field generated by the [6] and the [7] numerical schemes, respectively. The shock wave is well captured, good symmetry properties are observed and the tangency and impermeability conditions are well satisfied.

3.2.2. Viscous, unstructured and first-order accurate case – Same sense

Figures 10 and 11 exhibit the pressure contours obtained by the [6-7] schemes, respectively. The most severe pressure field is generated by the [6] scheme, with a pressure peak of approximately 166 unities. Better symmetry properties than in the inviscid case are observed in both solutions.

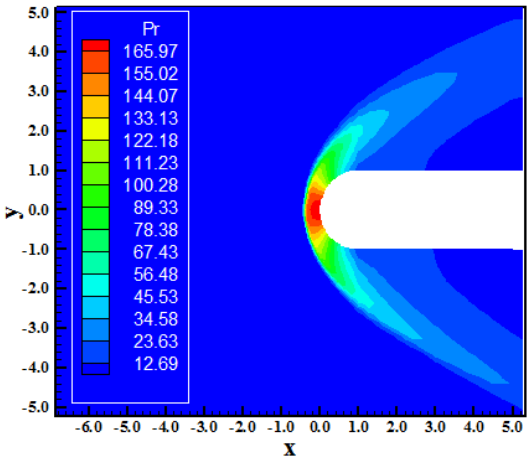

Figure 10. Pressure Contours (VL).

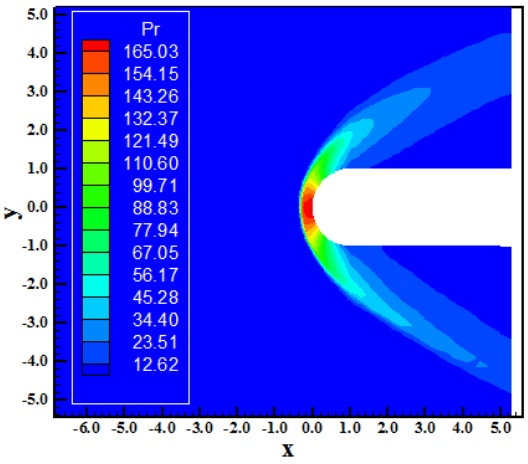

Figure 11. Pressure Contours (LS).

Figures 12 and 13 show the Mach number contours obtained by the [6] and the [7] numerical schemes, respectively. The Mach number field generated by the [7] algorithm is more intense than that generated by the [6] algorithm. Good symmetry properties are observed in both solutions. The shock wave is well captured by both schemes. The Mach wave develops naturally: passing from a normal shock wave at the blunt nose to oblique shock waves close to the body and to Mach waves far from

the body. The region of low Mach number along the blunt body demonstrates that the adherence and impermeability conditions were guaranteed. In the [7] solution, this region is not observed, which means that the adherence conditions is not satisfied.

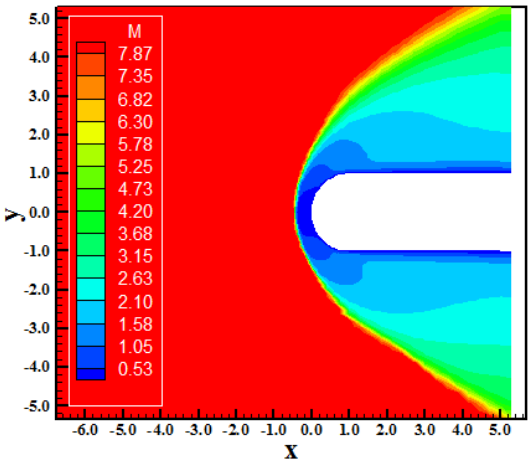

Figure 12. Mach Number Contours (VL).

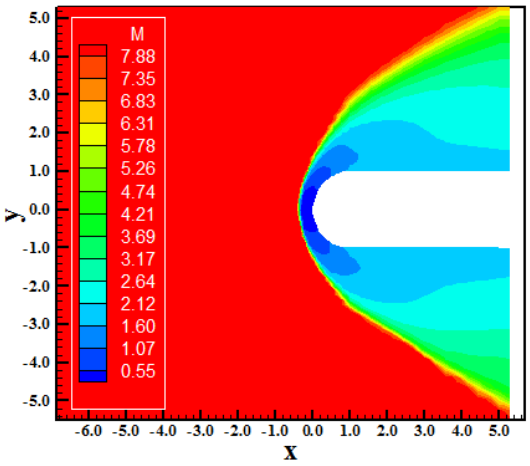

Figure 13. Mach Number Contours (LS).

Figures 14 and 15 present the translational / rotational temperature contours to the viscous case, obtained by the [6-7] schemes, respectively. As can be observed, the temperature peak in the [6] solution exceeds 9,000 K close to the geometry, what represent the dissociation of O_2 and N_2 in this region. This was the expected behavior since the physical transport phenomena of viscosity and thermal conductivity were considered, taking into account adiabatic wall. The [7] solution presents a temperature peak of approximately 8,479 K, which also guarantees the dissociation of O_2 and N_2. Good symmetry characteristics are observed in both solutions.

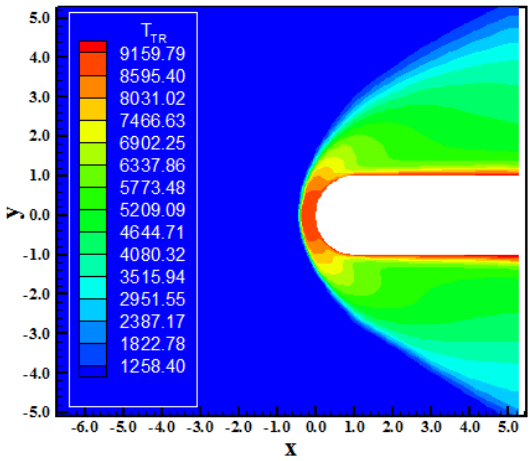

Figure 14. T/R Temperature Contours (VL).

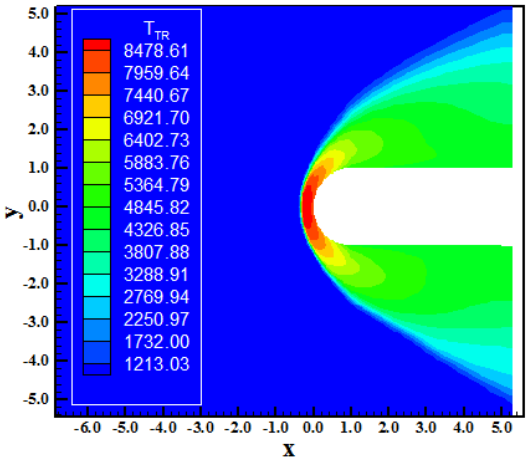

Figure 15. T/R Temperature Contours (LS).

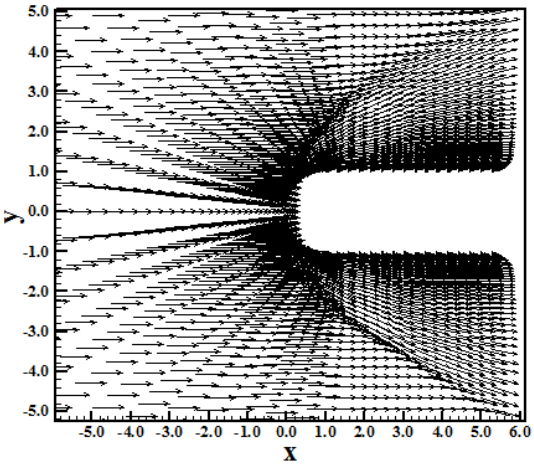

Figure 16. Velocity vector field (VL).

Figures 16 and 17 exhibit the velocity vector field obtained by the [6] and by the [7] algorithms, respectively. The shock wave is well captured by both schemes and good symmetry properties are

observed in both solutions. The adherence and impermeability conditions are well satisfied in the [6] solutions, whereas only the impermeability condition is well satisfied in the [7] scheme.

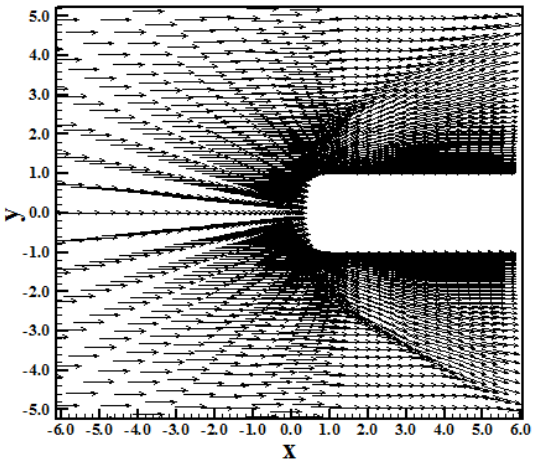

Figure 17. Velocity vector field (LS).

3.2.3. Inviscid, unstructured and first-order accurate case – Alternated sense

Figures 18 and 19 exhibit the pressure contours to the problem of the blunt body, employing the [6] and the [7] schemes, respectively. The [6] solution presents good characteristics of symmetry. The pressure peak is more severe in the [7] solution, as well the pressure field. This characterizes the [7] scheme as more conservative than the [6] scheme.

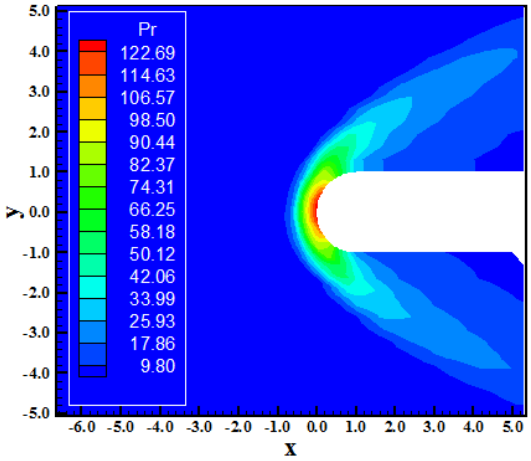

Figure 18. Pressure Contours (VL).

Figures 20 and 21 show the Mach number contours to this problem of the blunt body submitted to an inviscid flow. Good symmetry characteristics are observed in the [6] solution. Behind the normal shock, the flow becomes subsonic because of the intensity of this one. The shock wave behaves as expected: normal shock at the blunt nose, oblique shocks close to the body, and Mach waves far from the body.

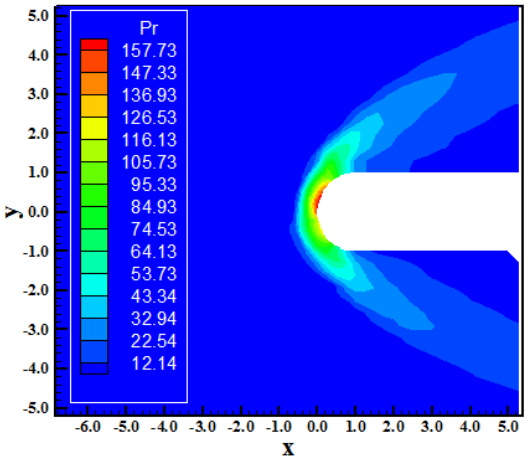

Figure 19. Pressure Contours (LS).

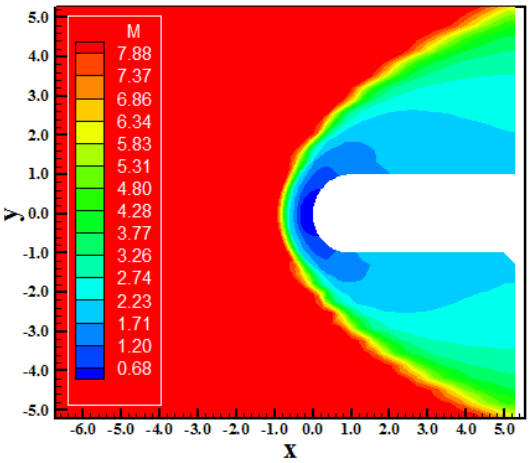

Figure 20. Mach Number Contours (VL).

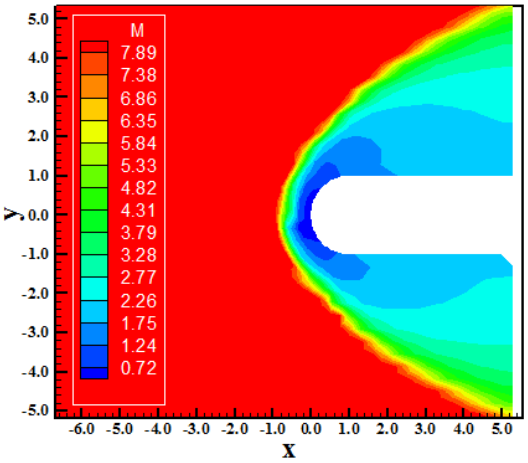

Figure 21. Mach Number Contours (LS).

Figures 22 and 23 present the translational / rotational temperature contours obtained by the [6]

and the [7] numerical algorithms, respectively. The temperature peak is superior to 8,100 K at the configuration nose, in the [6] solution, what express a bigger dissociation of O_2 and N_2 in this region.

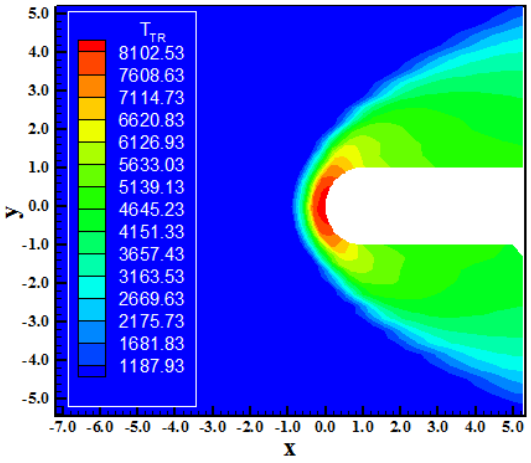

Figure 22. T/R Temperature Contours (VL).

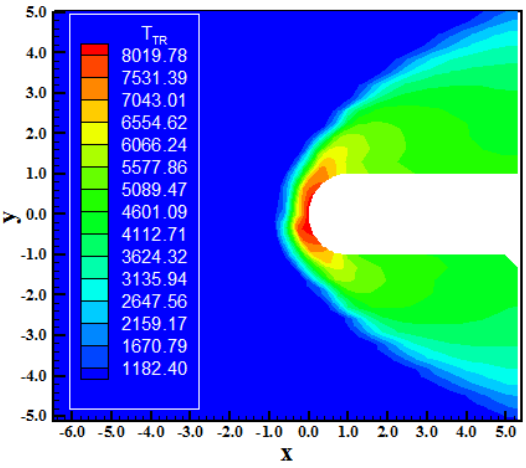

Figure 23. T/R Temperature Contours (LS).

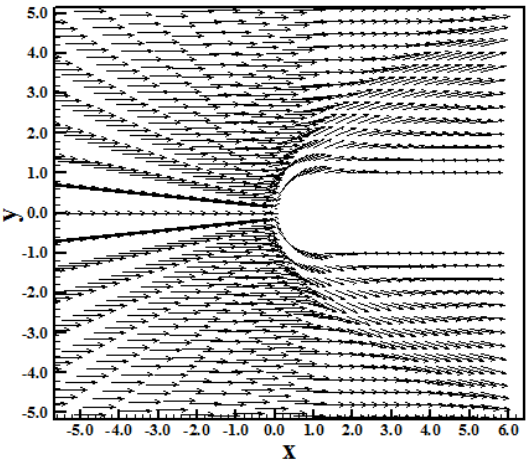

Figure 24. Velocity Vector Field (VL).

It is also possible to observe that due to the not formulation of transport mechanisms, like viscosity, thermal conductivity and species diffusion (Fick law), the temperature peak stays confined to the configuration-nose region, does not propagating along the blunt body, as expected to a inviscid formulation.

Figures 24 and 25 exhibit the velocity vector field obtained by the [6-7] algorithms, respectively. The shock wave is well captured by the numerical schemes. The tangency and impermeability conditions are also well satisfied by the numerical schemes.

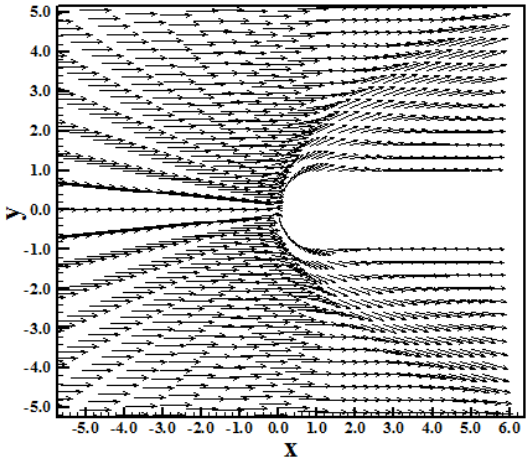

Figure 25. Velocity Vector Field (LS).

3.2.4. Viscous, unstructured and first-order accurate case – Alternated sense

Figures 26 and 27 show the pressure contours to the problem of the blunt body, in two-dimensions, considering viscous flow simulated with the [6] and the [7] schemes, respectively. The pressure fields are in general more severe than the respective ones due to the inviscid solution.

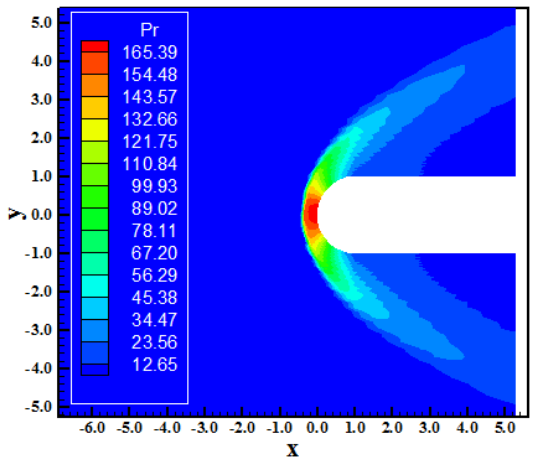

Figure 26. Pressure Contours (VL).

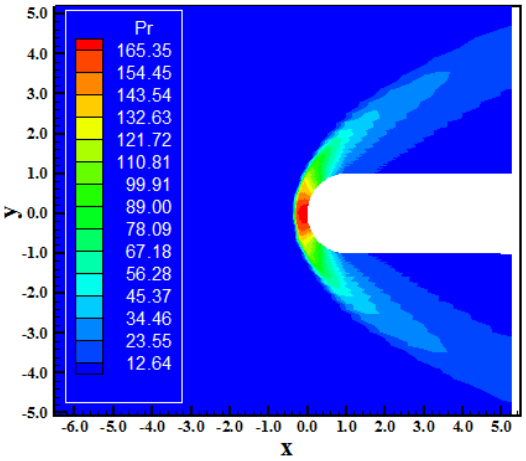

Figure 27. Pressure Contours (LS).

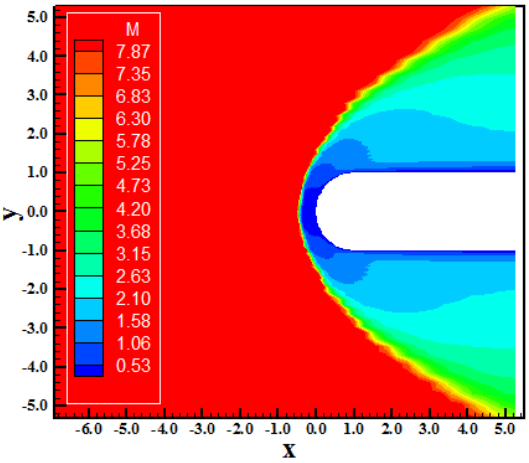

Figure 28. Mach Number Contours (VL).

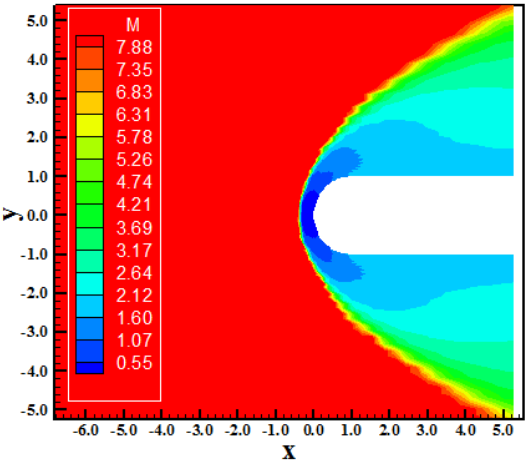

Figure 29. Mach Number Contours (LS).

The Mach number contours are exhibited in Figs. 28 and 29. They present good symmetry characteristics and the shock wave is closer to the nose than the inviscid solution. It is due to the employed mesh stretching and due to the reactive effects of the viscous simulation.

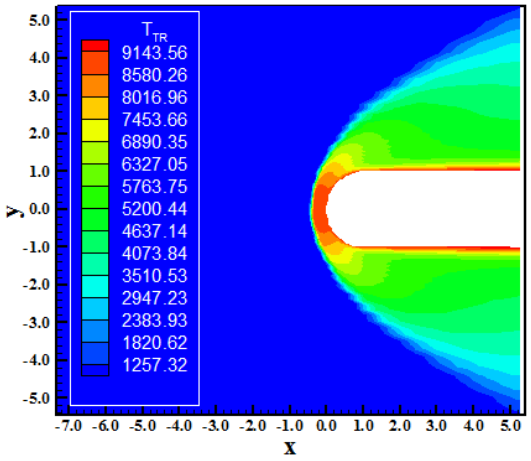

Figure 30. T/R Temperature Contours (VL).

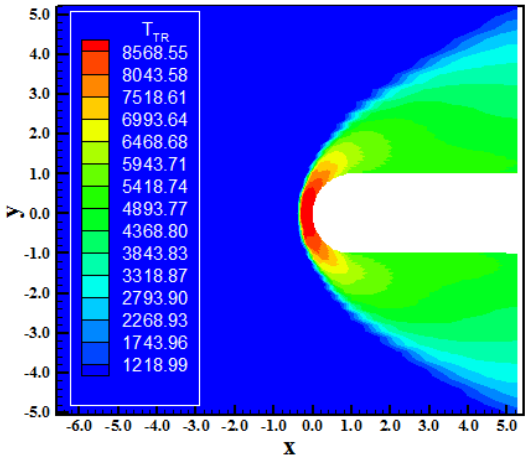

Figure 31. T/R Temperature Contours (LS).

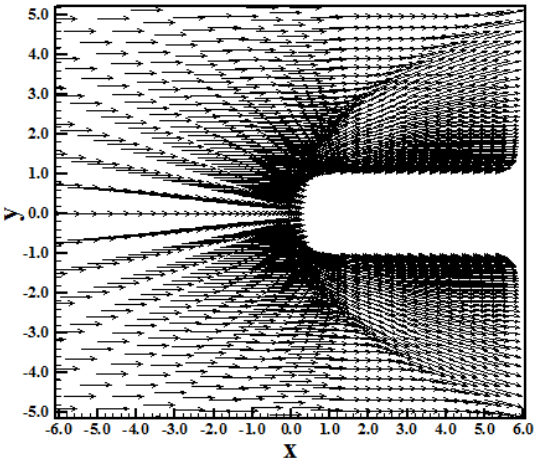

Figure 32. Velocity Vector Field (VL).

As can also be observed in the [6] solution, the region of low velocity propagates along the blunt

body, satisfying the conditions of adherence and impermeability of the viscous formulation. The same is not true to the [7] solution.

Figures 30 and 31 present the translational / rotational temperature distribution in the computational domain generated by the [6-7] schemes, respectively. The translational / rotational temperature peak is approximately 9,144 K to the [6] scheme and 8,569 K to the [7] scheme. The influence of the translational / rotational temperature is confined to a very much restrict region, which corresponds to the boundary layer, due to the consideration of the transport phenomena (viscosity, thermal conductivity and species diffusion).

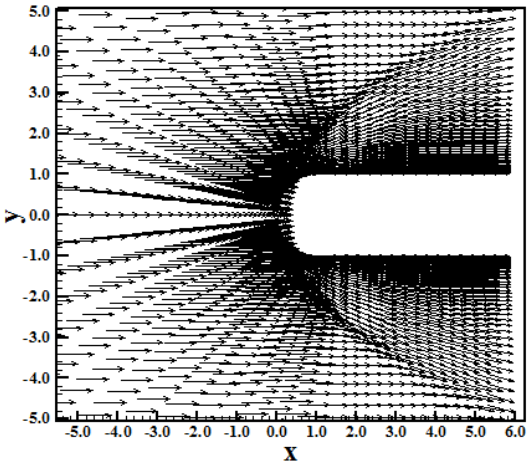

Figure 33. Velocity Vector Field (LS).

Figures 32 and 33 present the velocity vector field in this viscous case obtained by the [6] and the [7] algorithms, respectively. Both solutions present good symmetry properties. The numerical schemes captured the bow shock wave ahead of the blunt nose. It develops naturally: normal shock at the blunt nose, oblique shock waves close to the body, and Mach waves far from the body. The [7] scheme did not satisfy the adherence condition, only assuring impermeability condition. On the other hand, the [6] scheme satisfies the adherence and impermeability conditions.

3.3. Double ellipse results

Continuing this work, the second geometry under study consists in a double ellipse, trying to approximate the shuttle configuration. Details of the present configuration are obtained in [12]. Table 3 presents the initial condition adopted for this problem. This initial condition is more severe than the respective one to the blunt body problem.

Table 3. Initial conditions to the problem of the double ellipse.

Property	Value
M_∞	15.0
ρ_∞	0.00922 kg/m^3
p_∞	794.0 Pa
U_∞	5,208 m/s
T_∞	300.0 K
Altitude	50,000 m
c_N	10^{-9}
c_O	0.07955
c_{O2}	0.13400
c_{NO}	0.05090
L	5.0 m
Re_∞	1.574x10^6

3.3.1. Inviscid, structured and first-order accurate case

Figures 34 and 35 exhibit the pressure contours around the double ellipse in the computational domain generated by the [6-7] algorithms. The pressure field obtained by the [6] and the [7] schemes are the same in qualitative and quantitative aspects.

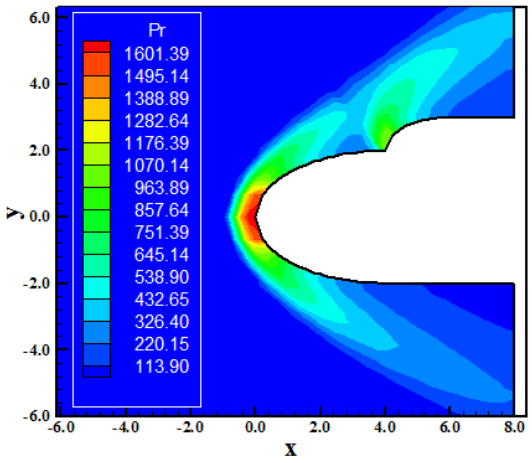

Figure 34. Pressure Contours (VL).

Figures 36 and 37 show the Mach number contours in the computational domain obtained by the [6] and the [7] algorithms. The Mach number field is the same as in qualitative aspects as in quantitative aspects. A region of subsonic flow is formed at the configuration nose due to the shock wave in this region be normal. The shock contours present the expected behavior: normal shock at the blunt body nose, being attenuated until reach a Mach wave configuration, far from the geometry. This Mach wave is obtained through successive oblique shock waves acting over the normal shock.

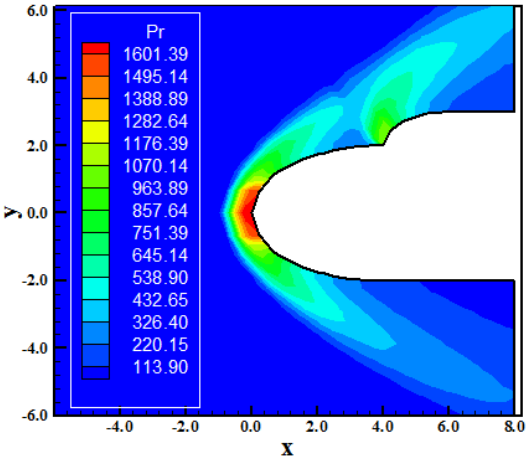

Figure 35. Pressure Contours (LS).

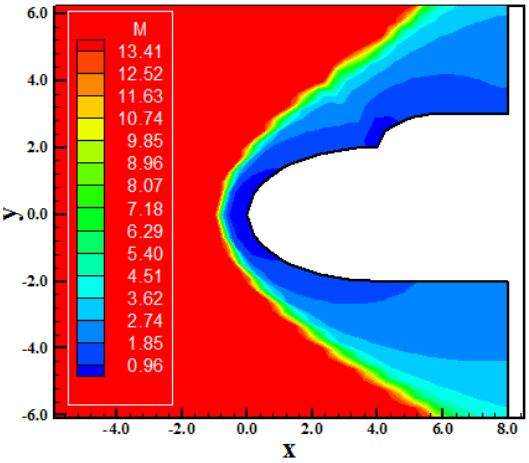

Figure 36. Mach Number Contours (VL).

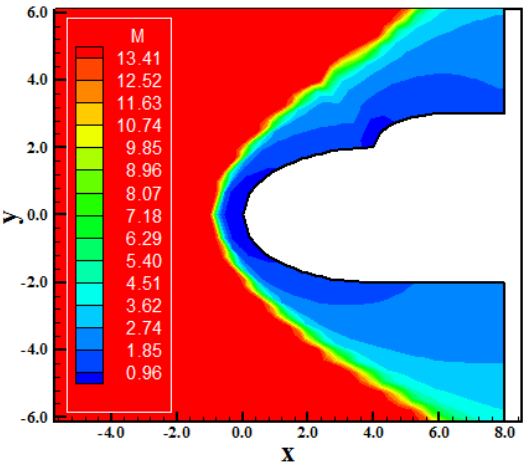

Figure 37. Mach Number Contours (LS).

Figures 38 and 39 present the translational / rotational temperature contours obtained by the [6] and the [7] algorithms, respectively. Both temperature fields are the same as in qualitative aspects as in quantitative aspects. The temperature peak is about 7,727 K, which assures the dissociation of N_2 and O_2, with the consequent increase in the N, O and NO mass fractions.

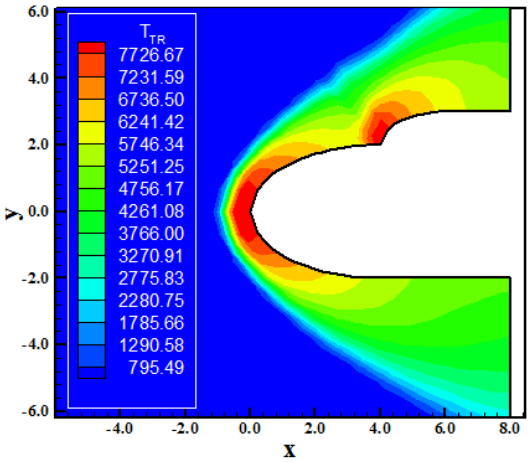

Figure 38. T/R Temperature Contours (VL).

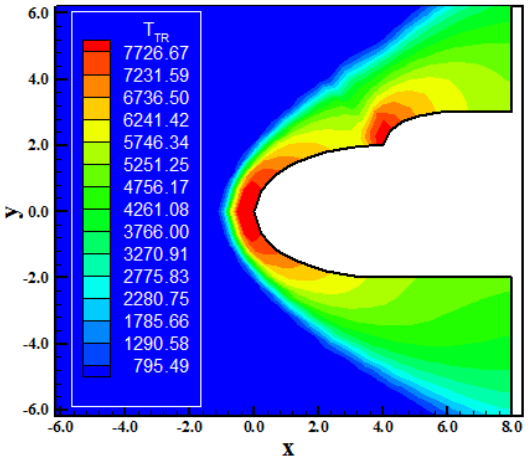

Figure 39. T/R Temperature Contours (LS).

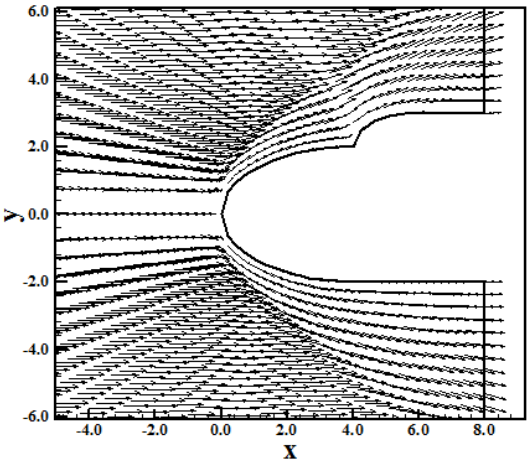

Figure 40. Velocity Vector Field (VL).

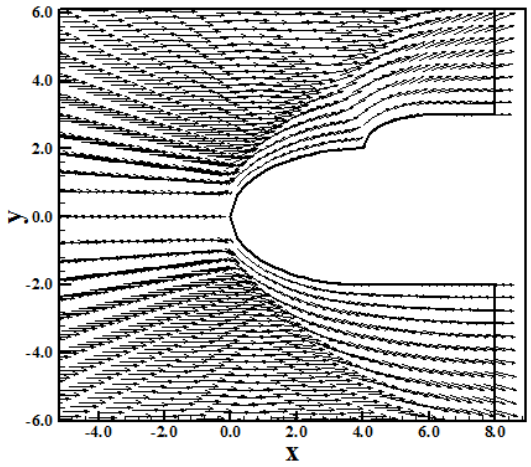

Figure 41. Velocity Vector Field (LS).

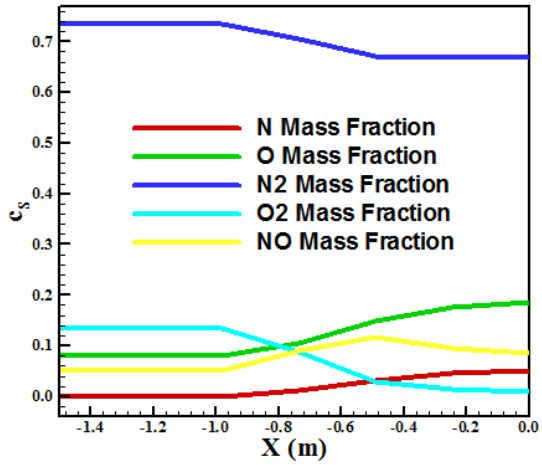

Figure 42. Mass fraction distributions at the stagnation line (VL).

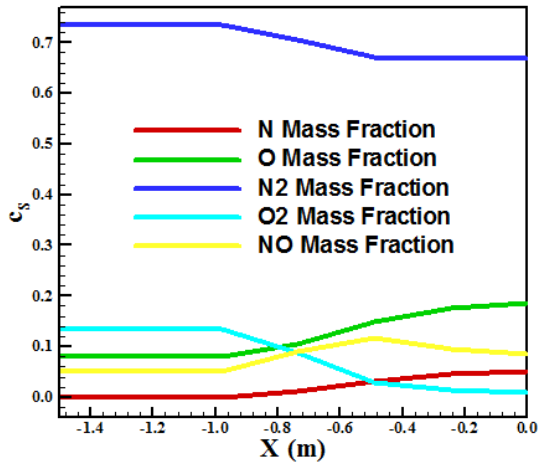

Figure 43. Mass fraction distributions at the stagnation line (LS).

Figures 40 and 41 exhibit the velocity vector fields generated by the [6-7] schemes, respectively. The bow shock wave is well captured by both algorithms. The tangency and impermeability conditions are well satisfied by the numerical schemes.

Figures 42 and 43 show the mass fraction distribution of the five chemical species studied in this work, namely: N, O, N_2, O_2, and NO along the line of stagnation of the blunt body. These distributions were obtained by the [6-7] schemes. As can be observed, an increase in the formation of the NO, of O and of N, with the respective reduction in the N_2 and O_2 species due to dissociation, occurs. The formation of O behind the shock, particularly, is more meaningful than the others due to the fact of the considerable dissociation of O_2.

3.3.2. Viscous, structured and first-order accurate case

Figures 44 and 45 present the pressure contours obtained in the computational domain by the [6] and the [7] schemes, respectively. Both pressure fields are exactly the same, in qualitative and quantitative aspects.

Figures 46 and 47 exhibit the Mach number contours generated by the [6-7] schemes, respectively. The shock wave behaves as expected: normal at the blunt body nose and attenuated until reaches a Mach wave configuration, far from the geometry under study. Both Mach number fields are the same as in qualitative aspects as in quantitative aspects. The peak of Mach number is formed at the blunt nose, in both solutions.

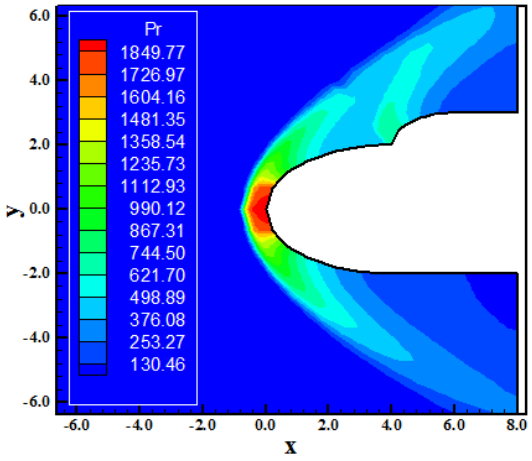

Figure 44. Pressure Contours (VL).

Figures 48 and 49 show the translational / rotational temperature contours obtained by the [6] and by the [7] numerical schemes, respectively. Both temperature fields are the same in qualitative and quantitative aspects. The temperature peak

reaches the value of 8,445 K, which guarantees good N_2 and O_2 dissociation.

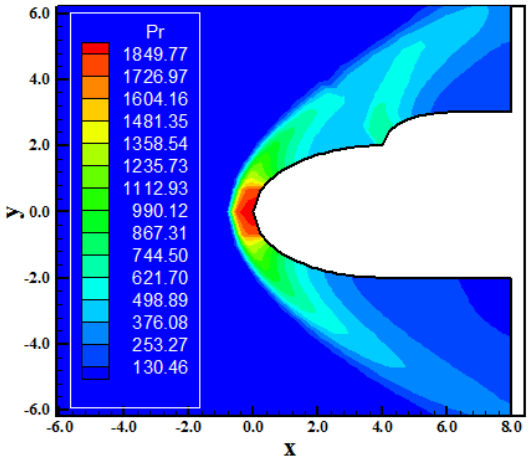

Figure 45. Pressure Contours (LS).

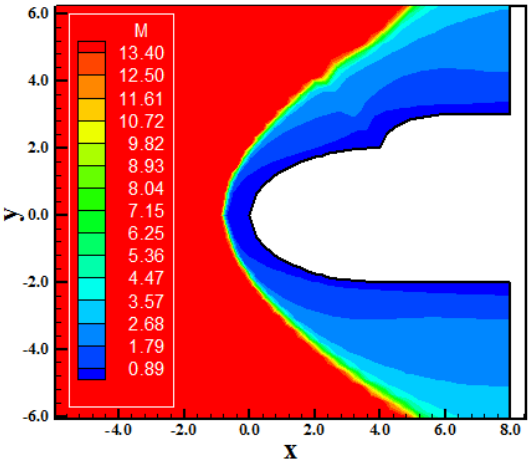

Figure 46. Mach Number Contours (VL).

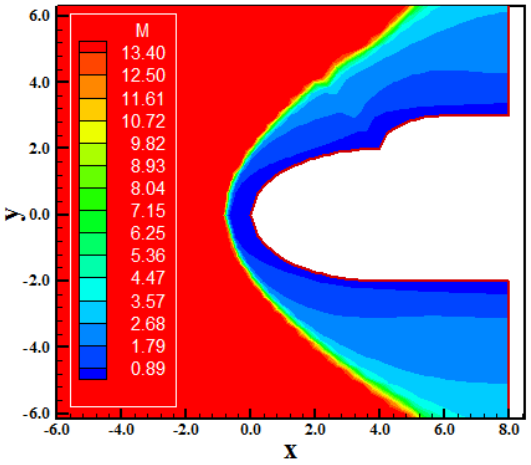

Figure 47. Mach Number Contours (LS).

Figures 50 and 51 present the velocity vector field obtained by the [6] and the [7] numerical algorithms, respectively. The bow shock wave has a good development, passing from a normal shock to oblique shock waves and reaching Mach waves far from the body. The adherence and impermeability conditions are well satisfied by both algorithms.

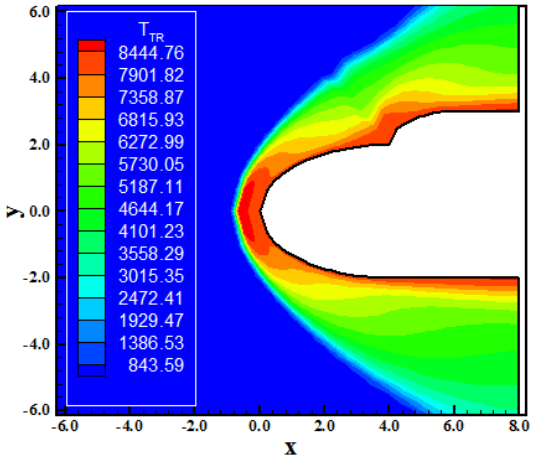

Figure 48. T/R Temperature Contours (VL).

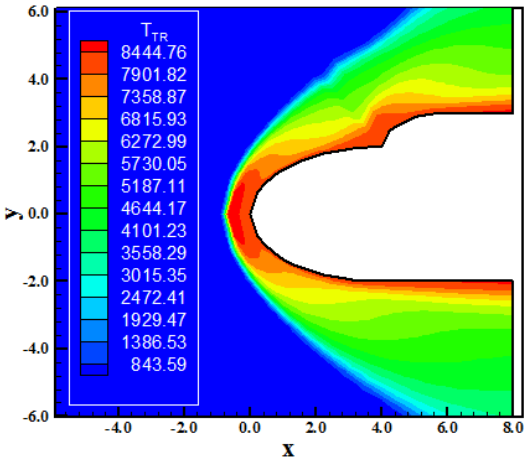

Figure 49. T/R Temperature Contours (LS).

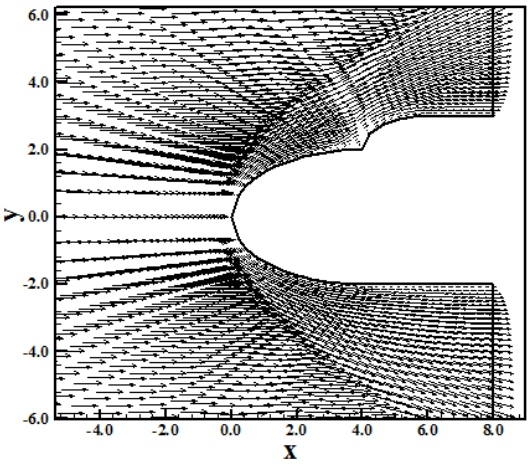

Figure 50. Velocity Vector Field (VL).

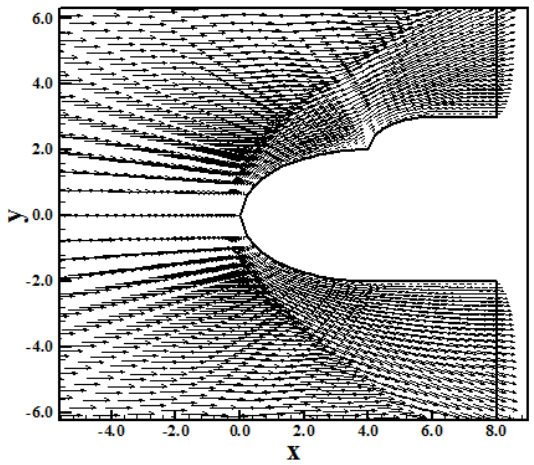

Figure 51. Velocity Vector Field (LS).

Figure 52 presents the mass fraction distribution of the five species in this chemical non-equilibrium flow obtained by the [6] scheme. Good dissociation of N_2 and O_2 are observed in this solution. The great increase of O mass fraction, as well of N is highlighted. Even the NO increase in mass fraction is emphasized as a good result.

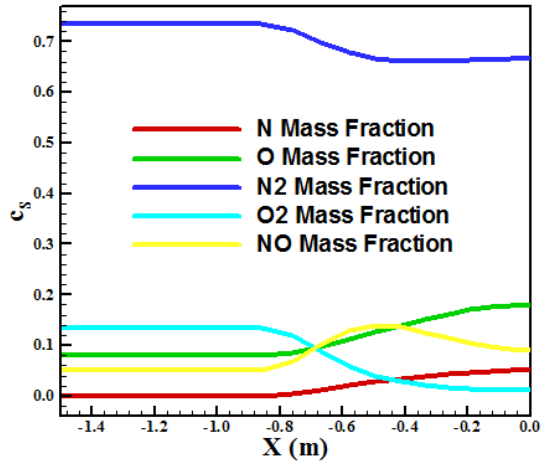

Figure 52. Mass fraction distributions at the stagnation line (VL).

Figure 53 exhibit the mass fraction distribution along the body's stagnation line obtained by the [6] and by the [7] numerical algorithms, respectively. Good dissociation of N_2 and O_2 is detected with consequent increase in the O, N and NO formations. The NO presents a reduction in its mass fraction distribution close to the blunt nose. This is because the N_2 dissociation that reaches a plateau and the same is true for the O_2 dissociation. Hence, the reduction in the formation of NO species results in a competition involving N and O, where they can choose between stay isolated as atoms or combine with themselves. Some choose to recombine and some to be isolated.

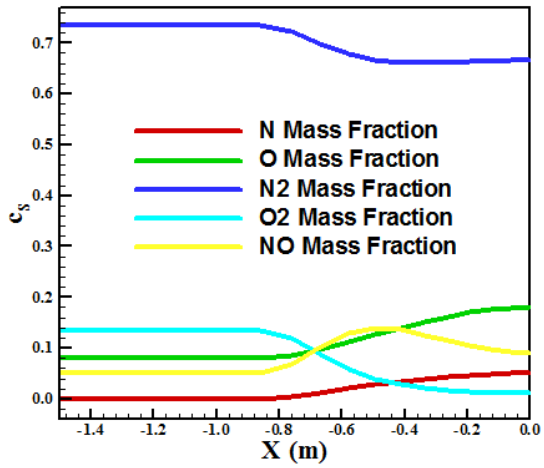

Figure 53. Mass fraction distributions at the stagnation line (LS).

3.3.3. Inviscid, structured and second-order accurate case

Figures 54 and 55 show the pressure contours obtained by the [6] and the [7] numerical algorithms, respectively. The same results are again observed in qualitative and quantitative terms. The pressure peak occurs at the blunt nose. The shock is well captured by both schemes.

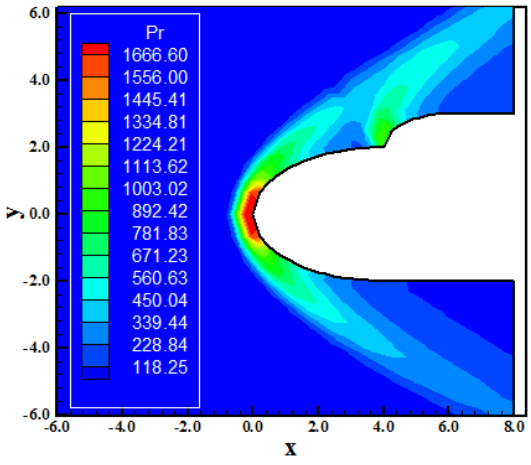

Figure 54. Pressure Contours (VL).

Figures 56 and 57 present the Mach number field obtained by the [6] and the [7] algorithms, respectively. Both Mach number field are the same, without meaningful differences. The shock wave is well captured where the presence of normal shock wave, oblique shock waves and Mach waves are perceptible. Behind the normal shock wave appears

a region of subsonic flow, typical of hypersonic flows around blunt geometries.

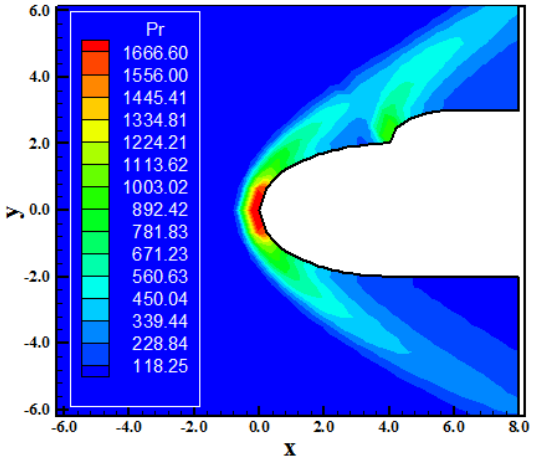

Figure 55. Pressure Contours (LS).

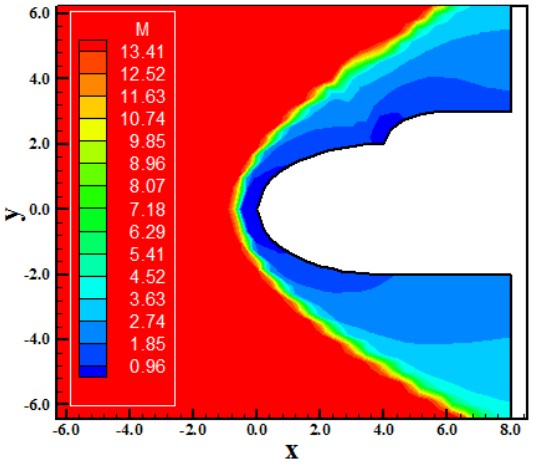

Figure 56. Mach Number Contours (VL).

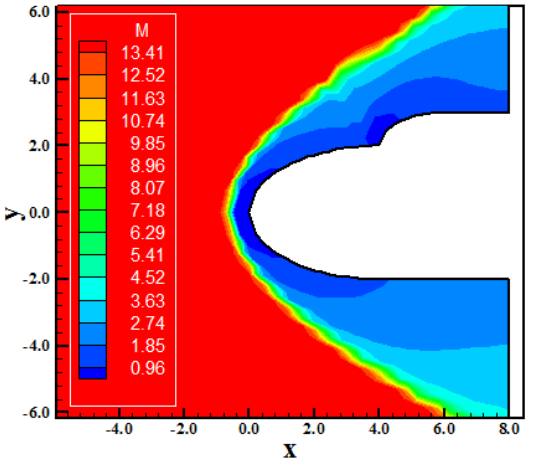

Figure 57. Mach Number Contours (LS).

Figures 58 and 59 exhibit the translational / rotational temperature contours generated by the [6] and the [7] algorithms, respectively. The same temperature field is observed in both solutions. The temperature peak reaches the value of 7,463 K, which assures N_2 and O_2 dissociations, with consequent increase in N, O and NO formations.

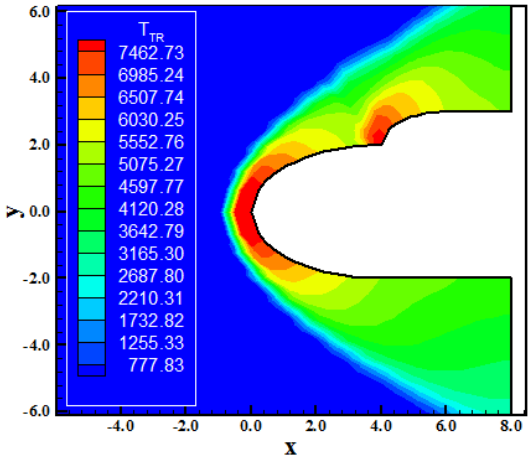

Figure 58. T/R Temperature Contours (VL).

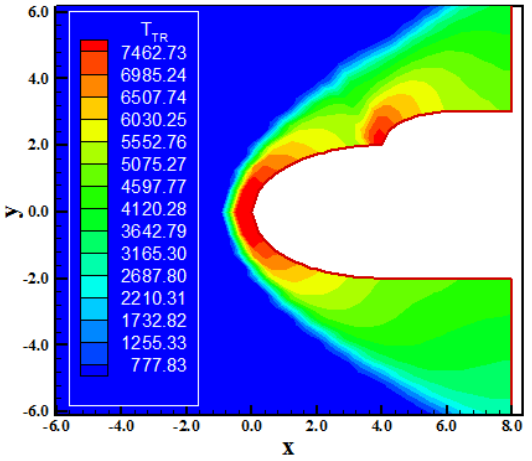

Figure 59. T/R Temperature Contours (LS).

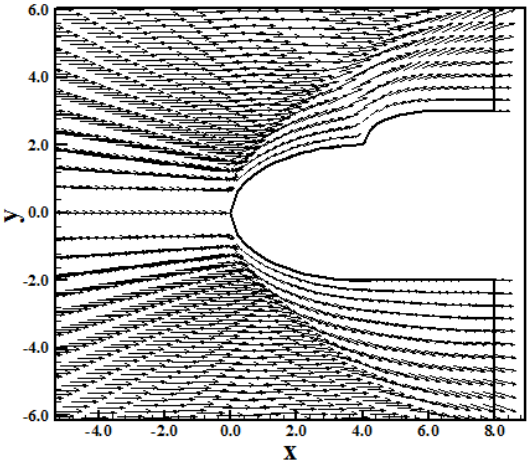

Figure 60. Velocity Vector Field (VL).

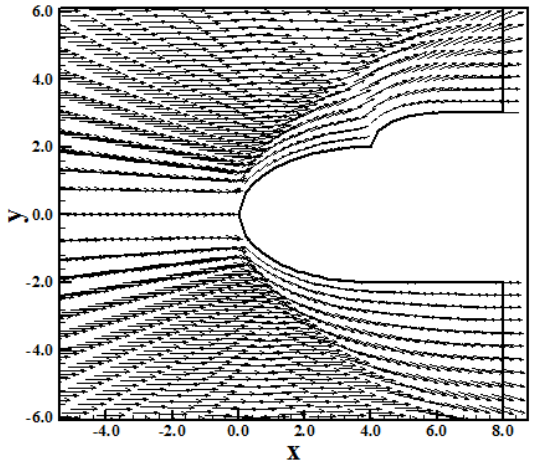

Figure 61. Velocity Vector Field (LS).

Figures 60 and 61 show the velocity vector field obtained by the [6] and the [7] schemes, respectively. The shock wave is well captured in both solutions and the tangency and impermeability conditions are well satisfied. The shock wave develops normally: normal shock, passing to oblique shock waves close to the body, and Mach waves far from the body.

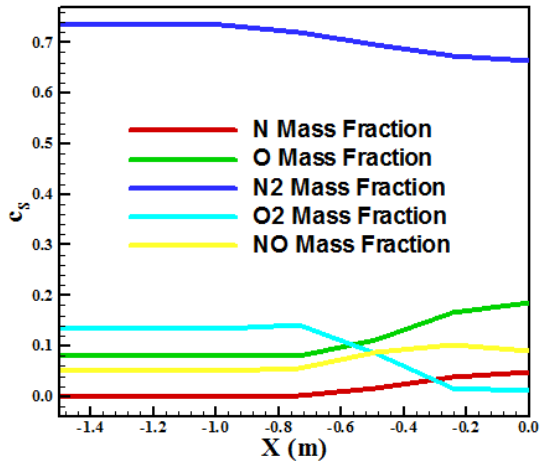

Figure 62. Mass fraction distributions at the stagnation line (VL).

Figures 62 and 63 present the mass fraction distributions generated by the [6] and the [7] schemes, describing the behavior of the five species under study. As can be observed, there is good dissociation of N_2 and O_2 along the line of stagnation, guaranteeing good formation of N, O and NO. The formation of N is also significant as observed in the other results. The formation of NO and O are excellent. The reduction in NO formation close to the body is a minimum because the N_2 and O_2 tend to reach a plateau close to the body and not far from the body.

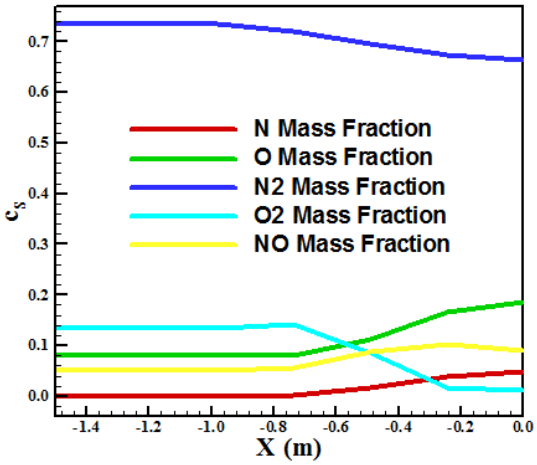

Figure 63. Mass fraction distributions at the stagnation line (LS).

3.3.4. Viscous, structured and second-order accurate case

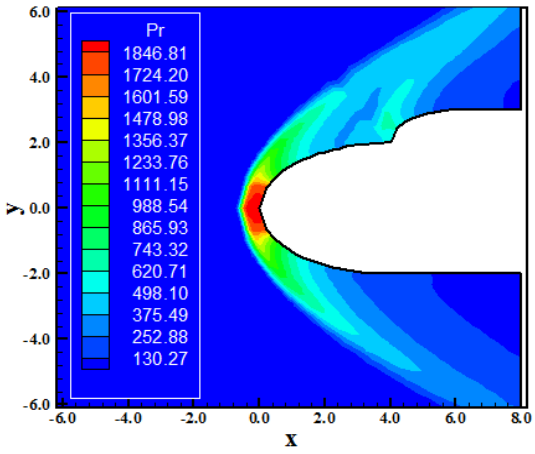

Figure 64. Pressure Contours (VL).

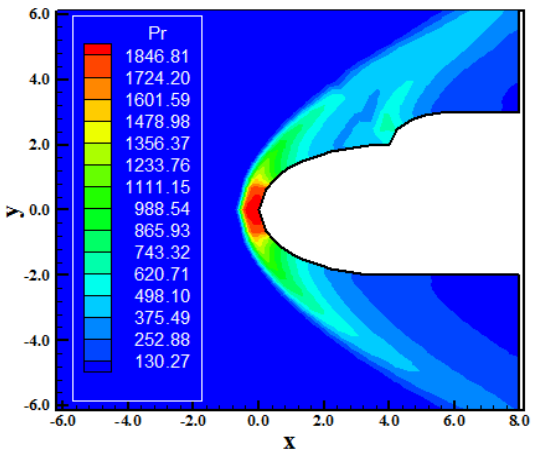

Figure 65. Pressure Contours (LS).

Figures 64 and 65 exhibit the pressure contours obtained by the [6-7] numerical algorithms, respectively. The same pressure field is obtained by the [6] and the [7] schemes. Figures 66 and 67 show the Mach number field obtained by both schemes. The same behavior observed before is repeated herein. The subsonic region after the shock wave propagates along the body and characterizes the slowdown of the flow due to the boundary layer presence.

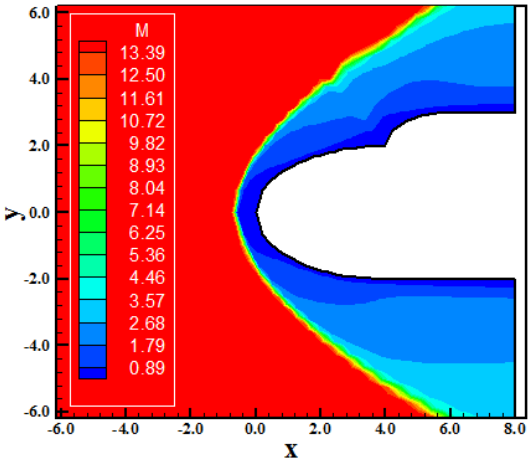

Figure 66. Mach Number Contours (VL).

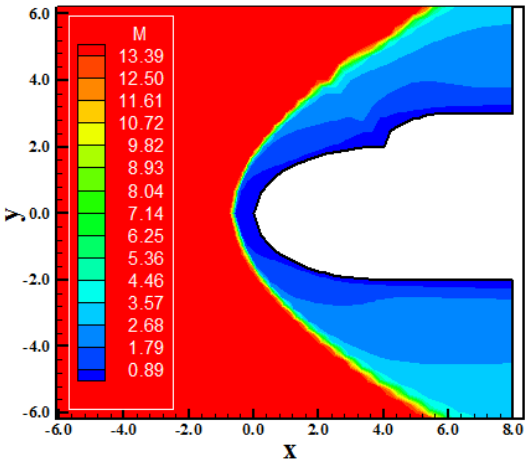

Figure 67. Mach Number Contours (LS).

Figure 68 and 69 present the translational / rotational temperature contours obtained by the [6-7] numerical algorithms. As can be observed the temperature peak reaches the value 8,409 K, which guarantees N_2 and O_2 dissociation, with consequent formation of N, O and NO.

Figures 70 and 71 exhibit the velocity vector field obtained by the [6] and by the [7] schemes, respectively. The shock is well captured by the numerical schemes, and the adherence and impermeability conditions are also well satisfied by the numerical algorithms. The shock wave develops normally: normal shock wave at the blunt nose, oblique shock waves close to the body, and Mach waves far from the body.

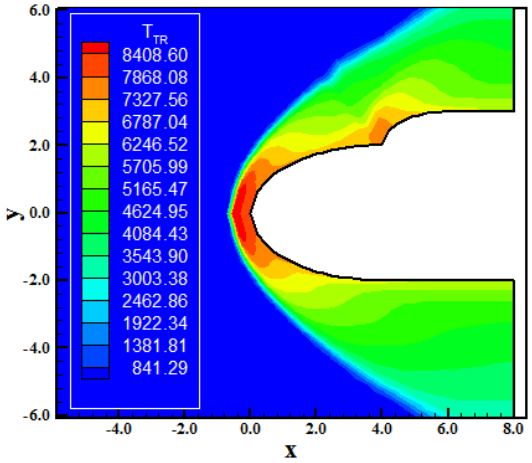

Figure 68. T/R Temperature Contours (VL).

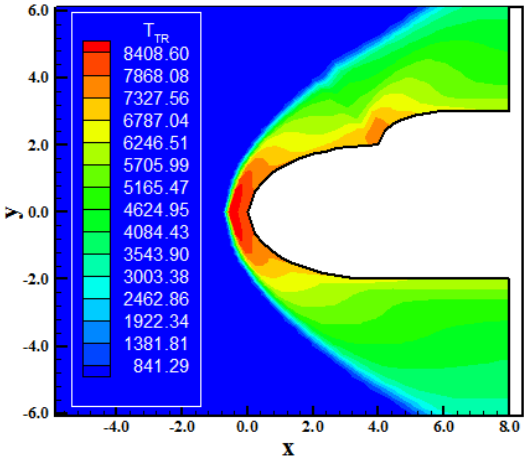

Figure 69. T/R Temperature Contours (LS).

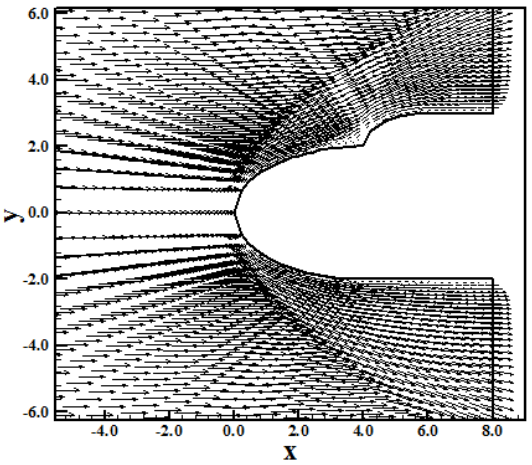

Figure 70. Velocity Vector Field (VL).

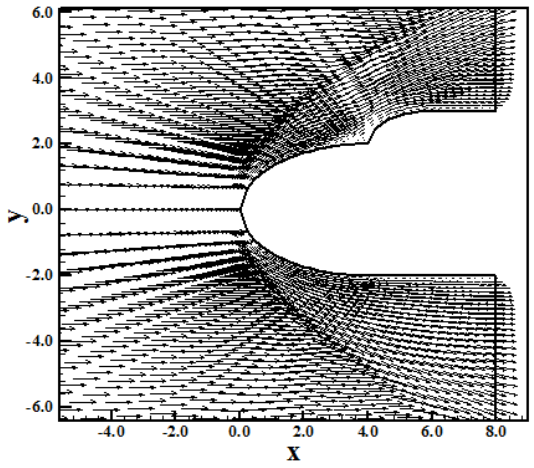

Figure 71. Velocity Vector Field (LS).

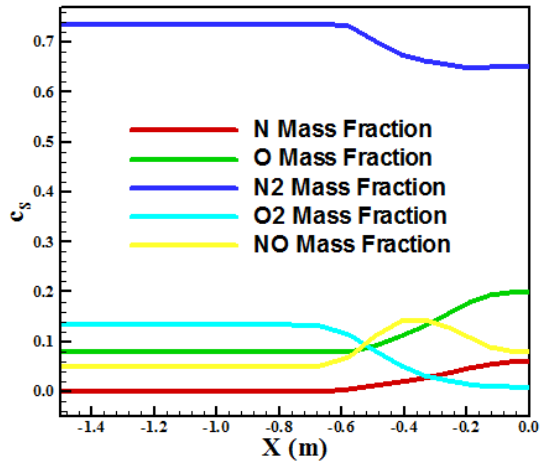

Figure 72. Mass fraction distributions at the stagnation line (VL).

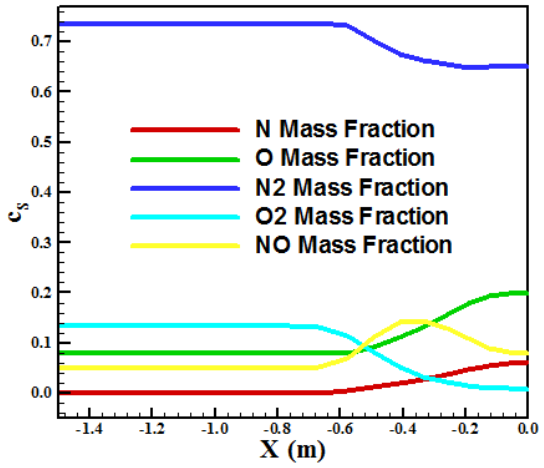

Figure 73. Mass fraction distributions at the stagnation line (LS).

Figures 72 and 73 exhibit the mass fraction distribution along the stagnation line obtained by the [6] and by the [7] numerical schemes. In both solutions, the N and O presented good increase in their formations. The NO presents an increase close to the body and a reduction at the blunt nose. It is due to the constancy in the dissociation of the N_2 and O_2 in this region, and the increase in the formation of N and of O, reducing, hence, the number of N and O available to the NO formation.

3.3.5.1. Inviscid, unstructured and first-order accurate case – Same sense

In this case, only the [6] scheme presented converged results. In Figure 74, the pressure contours are presented. Good capture of the shock wave is observed and the pressure peak reaches the value of 1,718 unities. The normal shock wave is well captured at the blunt nose. Figure 75 shows the Mach number field obtained by the [6] scheme. The Mach number peak reaches the value of 13.42. The shock wave develops normally: normal shock wave, oblique shock waves close to the body, and Mach wave far from the body. The subsonic region formed behind the shock wave is well captured.

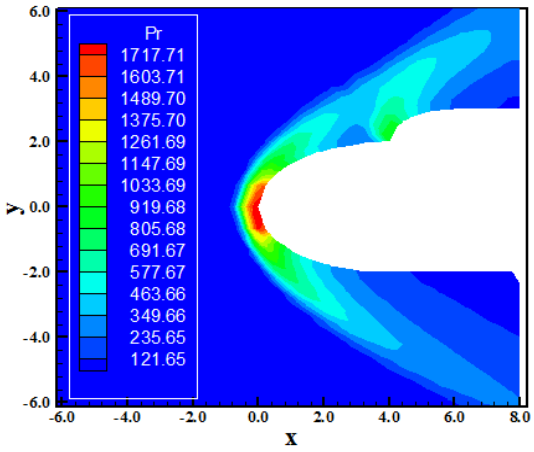

Figure 74. Pressure Contours (VL).

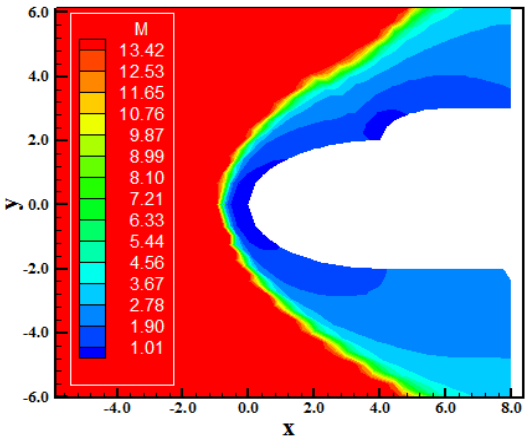

Figure 75. Mach Number Contours (VL).

Figure 76 presents the translational / rotational temperature contours obtained by the [6] scheme. The temperature peak reaches the value of 8,359 K, which assures the dissociation of N_2 and O_2. Figure 77 exhibits the velocity vector field obtained by the [6] scheme. The shock wave is well captured and the tangency and impermeability conditions are well satisfied by the numerical scheme.

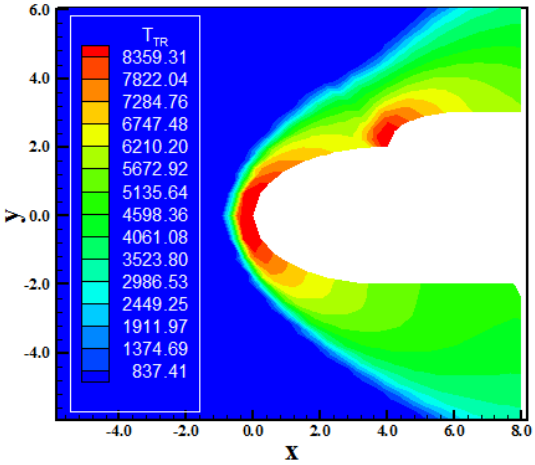

Figure 76. T/R Temperature Contours (VL).

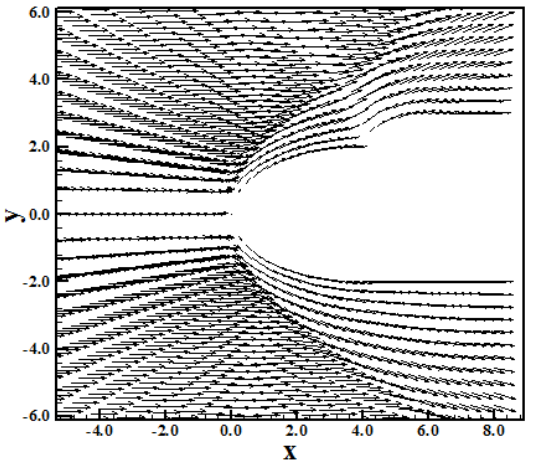

Figure 77. Velocity Vector Field (VL).

3.3.5.2. Viscous, unstructured and first-order accurate case – Same sense

In this case, only the [6] scheme presented converged results. Figure 78 shows the pressure contours with pressure peak equal to 1,891 unities. Moreover, the shock wave is well captured and the pressure peak occurs at the blunt nose. Figure 79 presents the Mach number field generated by the [6] scheme. The shock wave is well captured and this one behaves as expected. The subsonic region behind the normal shock wave is also well captured. This subsonic region propagates along the body wall, due to the transport properties taken into account. Figure 80 exhibits the translational / rotational temperature contours obtained by the [6] scheme. The temperature peak reaches the value of 8,955 K, which guarantees the N_2 and O_2 dissociations.

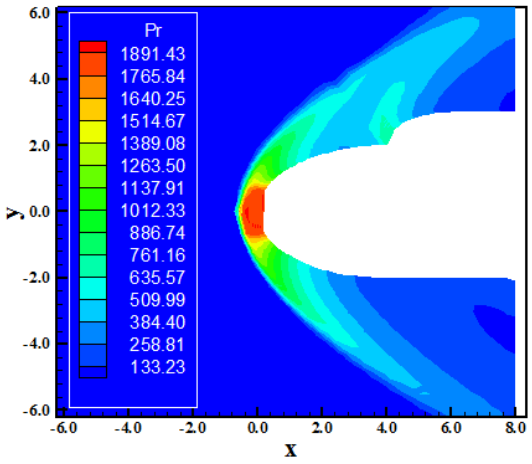

Figure 78. Pressure Contours (VL).

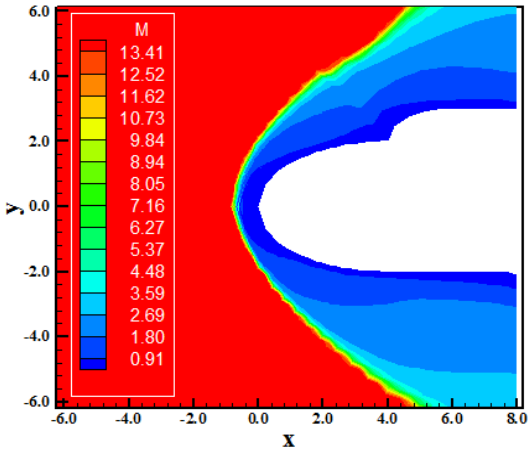

Figure 79. Mach Number Contours (VL).

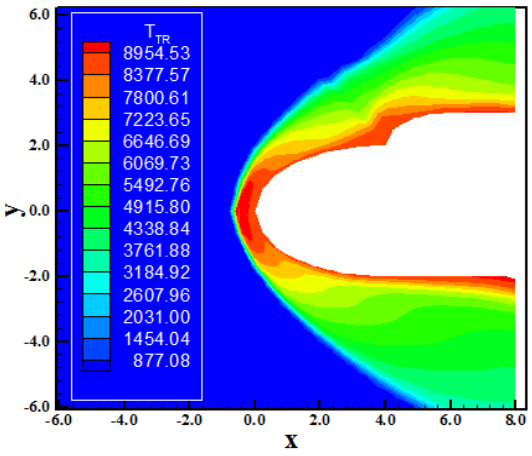

Figure 80. T/R Temperature Contours (VL).

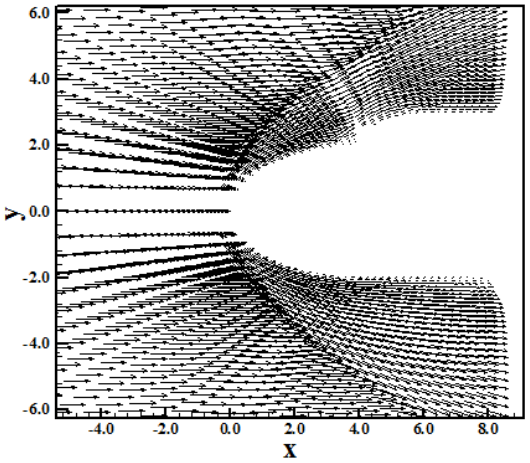

Figure 81. Velocity Vector Field (VL).

Figure 81 shows the velocity vector field obtained by the [6] scheme. Good capture of the bow shock wave is observed. The adherence and impermeability conditions are well satisfied.

3.3.5.3. Inviscid, unstructured and first-order accurate case – Alternated sense

In this case, only the [6] scheme presents converged results. The pressure contours is presented in Fig. 82. The pressure peak reaches the value of 1,706 unities and is located at the blunt nose. Both the first and the second shocks are well captured by the numerical scheme. Figure 83 exhibits the Mach number field obtained by the [6] scheme. The shock wave develops normally: normal shock at the configuration nose, oblique shock waves close to the body, and Mach waves far from the body. Figure 84 shows the translational / rotational temperature contours, which reaches a temperature peak of approximately 8,317 K, assuring N_2 and O_2 dissociations.

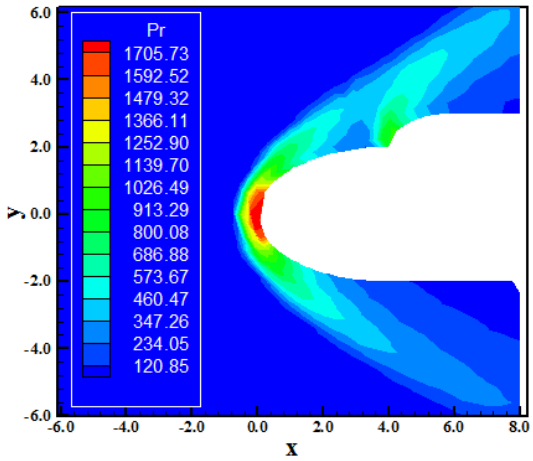

Figure 82. Pressure Contours (VL).

Finally, Figure 85 presents the velocity vector field obtained by the [6] scheme. The shock is well characterized, defining appropriately the shock wave behavior. The tangency and impermeability conditions are plenty satisfied.

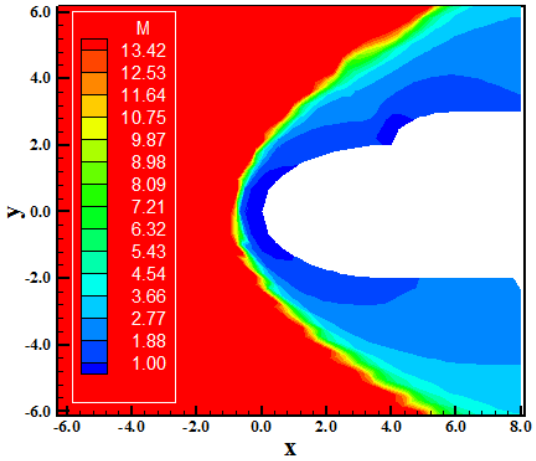

Figure 83. Mach Number Contours (VL).

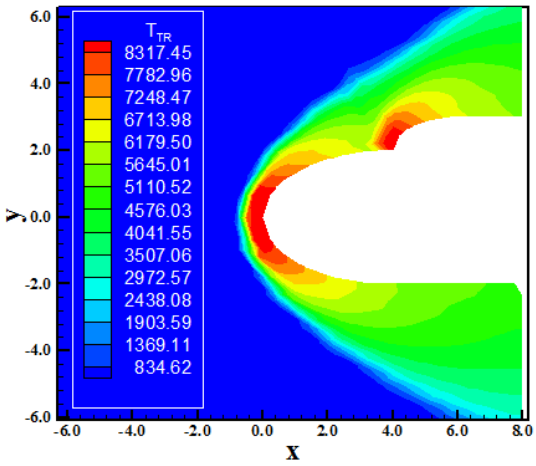

Figure 84. T/R Temperature Contours (VL).

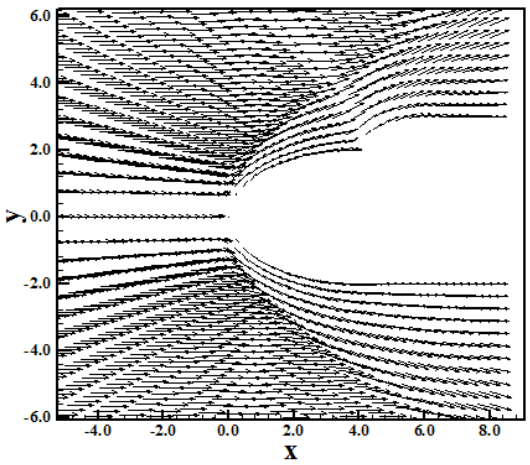

Figure 85. Velocity Vector Field (VL).

3.3.5.4. Viscous, unstructured and first-order accurate case – Alternated sense

Both schemes did not present converged results.

3.4. Re-entry capsule results

The re-entry capsule problem is another hypersonic test performed in this work. The initial conditions are presented below. Details of the present configuration are obtained in [12]. Table 4 presents the initial condition adopted for this problem. This initial condition is more severe than the respective one to the blunt body problem. Only the structured results are presented; the unstructured formulation has presented problems in the wake and is not exhibited.

Table 4. Initial conditions to the problem of the re-entry capsule.

Property	Value
M_∞	10.6
ρ_∞	0.02863 kg/m^3
p_∞	3,885 Pa
U_∞	4,628 m/s
T_∞	473 K
Altitude	40,000 m
c_N	10^{-9}
c_O	0.07955
c_{O2}	0.13400
c_{NO}	0.05090
L	3.0 m
Re_∞	3.468x10^6

3.4.1. Inviscid, structured and first-order accurate case

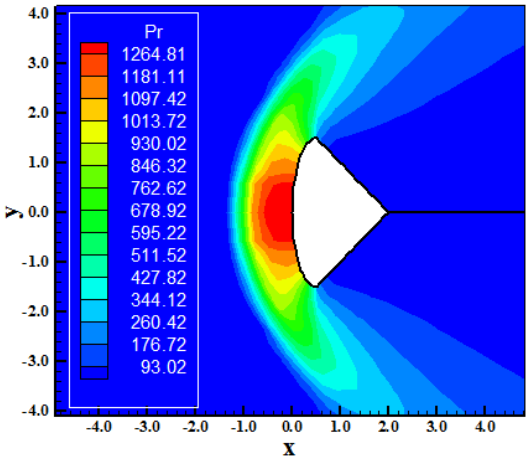

Figure 86. Pressure Contours (VL).

Figures 86 and 87 exhibit the pressure contours obtained by the [6] and the [7] schemes, respectively. Good symmetry properties are observed. The pressure field is essentially the same, demonstrating that the two algorithms converged to the same results. The solutions are equal as in qualitative terms as in quantitative terms.

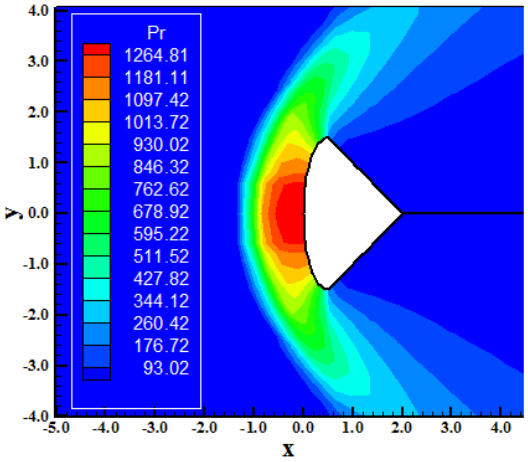

Figure 87. Pressure Contours (LS).

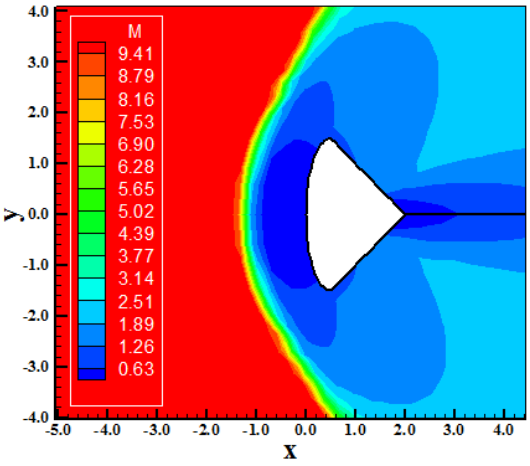

Figure 88. Mach Number Contours (VL).

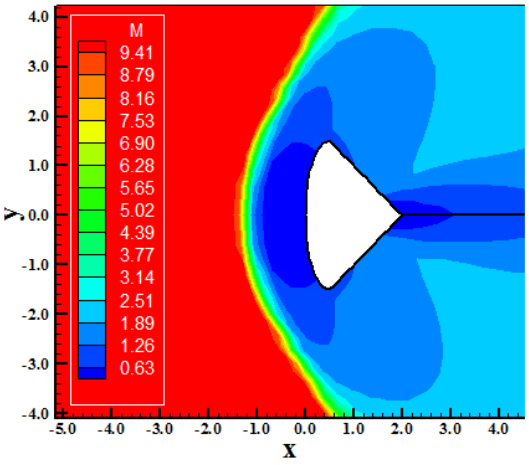

Figure 89. Mach Number Contours (LS).

Figure 88 and 89 show the Mach number contours generated by both schemes. Both solutions are the same, without meaningful discrepancies. Figures 90 and 91 present the translational / rotational temperature contours obtained by the [6-7] schemes, respectively.

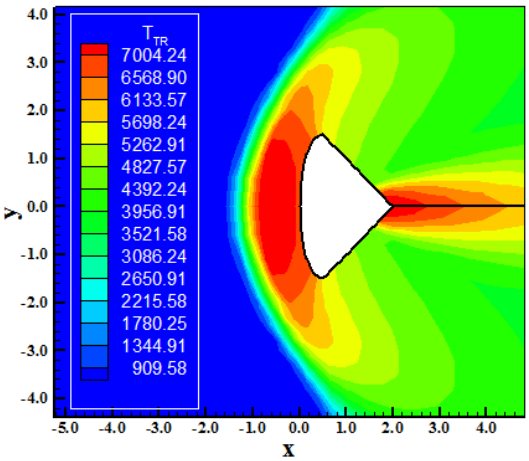

Figure 90. T/R Temperature Contours (VL).

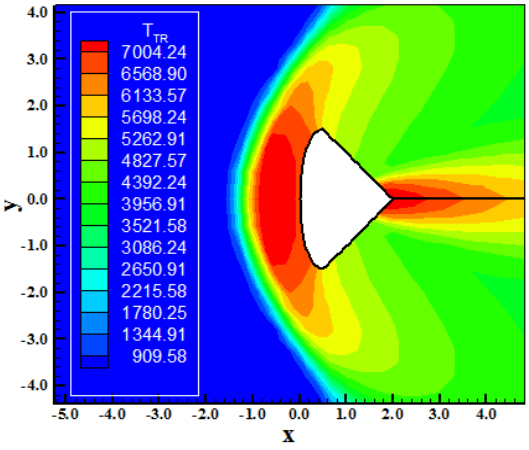

Figure 91. T/R Temperature Contours (LS).

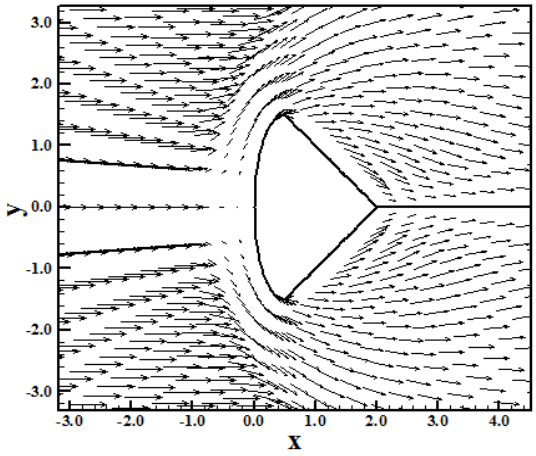

Figure 92. Velocity Vector Field (VL).

Both solutions present the same behavior, with a temperature peak of 7,004 K, which guarantees the N_2 and O_2 dissociations.

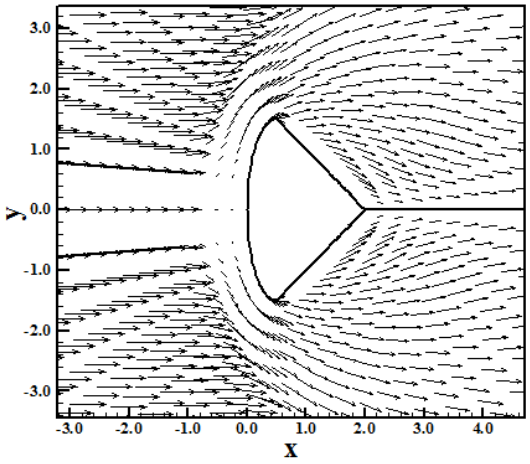

Figure 93. Velocity Vector Field (LS).

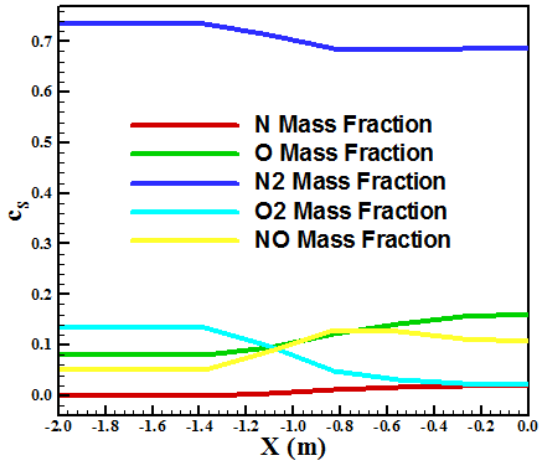

Figure 94. Mass fraction distributions at the stagnation line (VL).

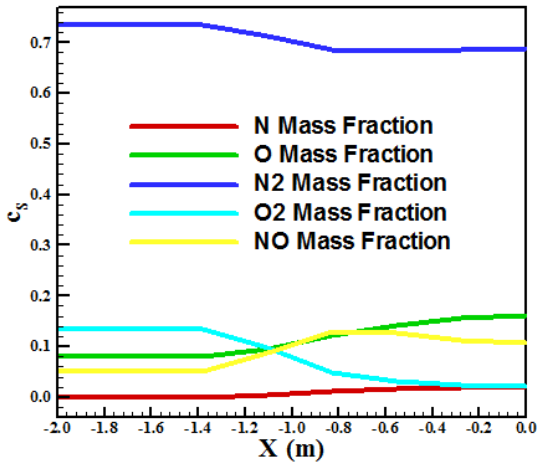

Figure 95. Mass fraction distributions at the stagnation line (LS).

Figures 92 and 93 exhibit the velocity vector field obtained by the [6-7] schemes, respectively. Good symmetry properties are observed. The impermeability and tangency conditions are well satisfied by both schemes.

Figures 94 and 95 show the mass fraction distributions, along the stagnation line of the re-entry capsule, obtained by the [6] and the [7] algorithms. Good formation of N and O is observed, with reasonable formation of NO. The same aspects observed for NO in other cases are valid herein. Both solutions are the same, without meaningful differences.

3.4.2. Viscous, structured and first-order accurate case

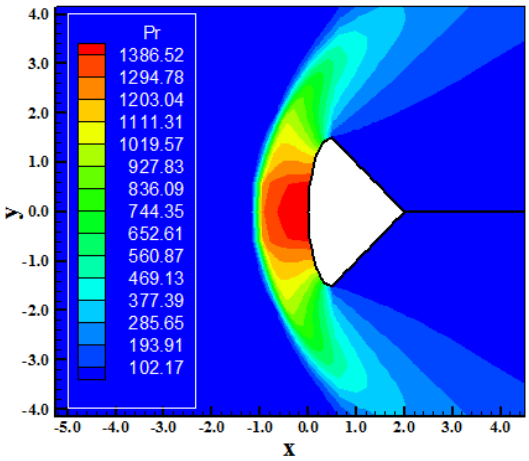

Figure 96. Pressure Contours (VL).

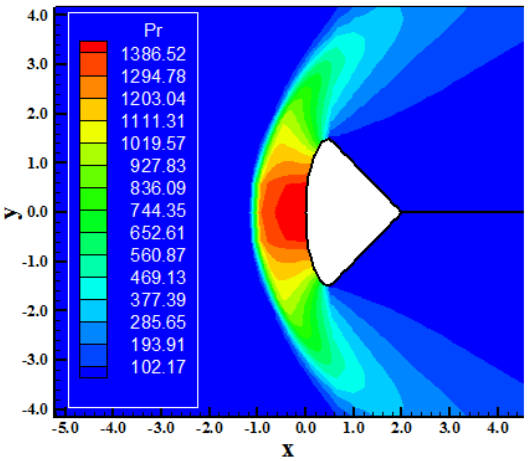

Figure 97. Pressure Contours (LS).

Figures 96 and 97 present the pressure contours generated by the [6] and the [7] algorithms, respectively. The solutions present the same behavior. Good symmetry properties are observed. The pressure peak assumes the value of 1,387 unities. Figures 98 and 99 exhibit the Mach number contours obtained by both schemes. Both schemes capture the bow shock wave with accuracy. The subsonic region formed behind the normal shock wave is well captured by both algorithms. The subsonic wake is also well captured by both schemes.

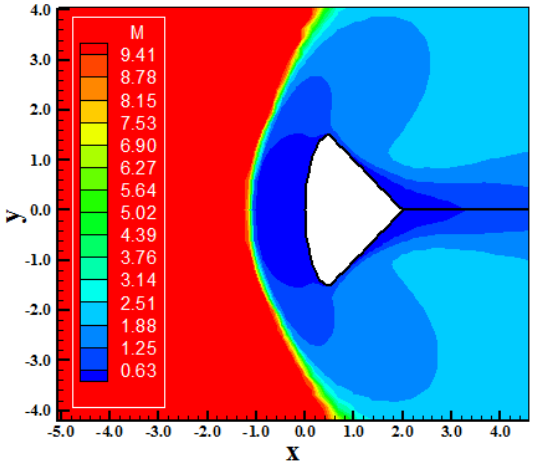

Figure 98. Mach Number Contours (VL).

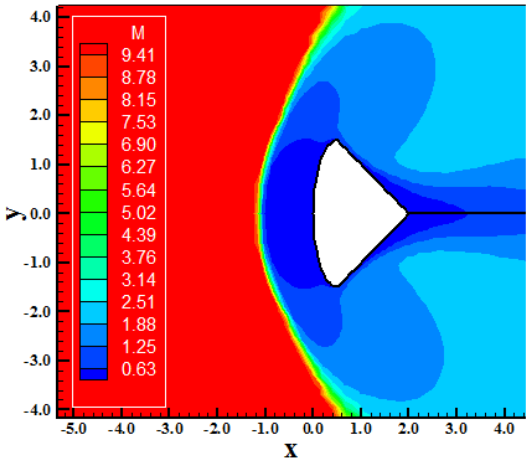

Figure 99. Mach Number Contours (LS).

Figures 100 and 101 show the translational / rotational temperature contours obtained by the [6] and the [7] algorithms. Both solutions capture the same temperature field and the temperature peak is 7,627 K, which assures N_2 and O_2 dissociations. Figures 102 and 103 present the velocity vector field close to the body trailing edge, where a pair of circulation bubbles is formed in this region. It is important to remember that behind the re-entry capsule exists the detachment of the boundary layer from the body due to adverse pressure gradient that appears in this region. It is the cause of the flow separation and the formation of circulation bubbles

in pair. Note that it is the region of intense loss of energy and variation of pressure and that the pair of bubbles is formed as a consequence of such mechanisms. Figures 104 and 105 exhibit the mass fraction distributions along the stagnation line of the re-entry capsule.

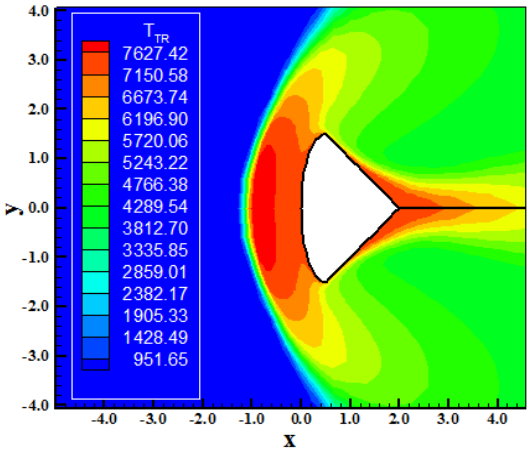

Figure 100. T/R Temperature Contours (VL).

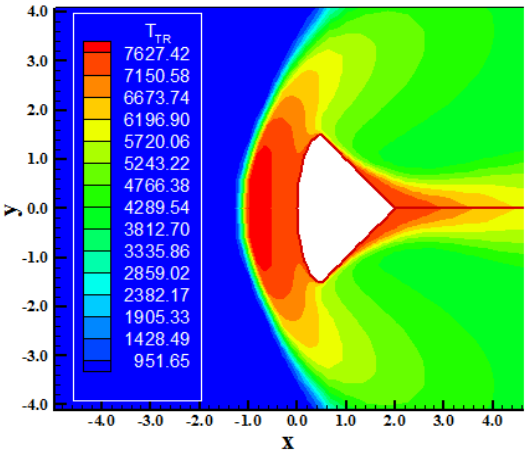

Figure 101. T/R Temperature Contours (LS).

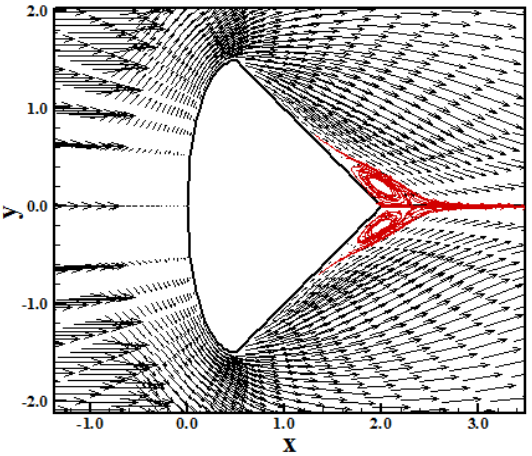

Figure 102. Velocity Vector Field (VL).

Good formation of N and O is observed. Good dissociation of N_2 and O_2 is also verified. The NO formation has the same behavior as in the cases before.

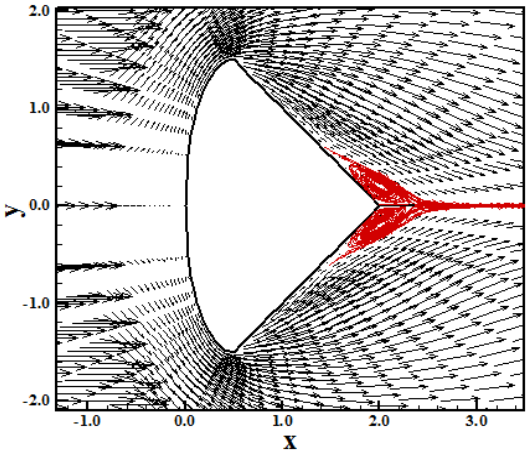

Figure 103. Velocity Vector Field (LS).

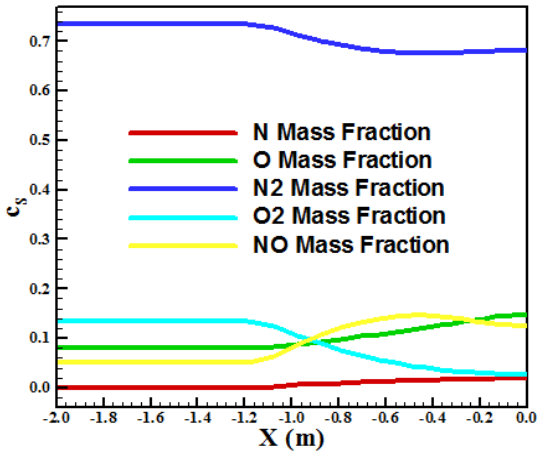

Figure 104. Mass fraction distributions at the stagnation line (VL).

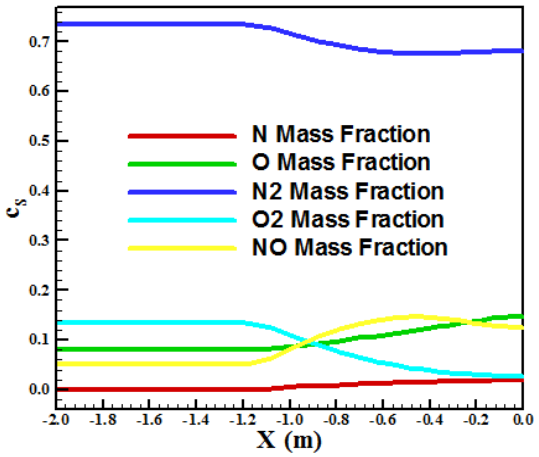

Figure 105. Mass fraction distributions at the stagnation line (LS).

3.4.3. Inviscid, structured and second-order accurate case

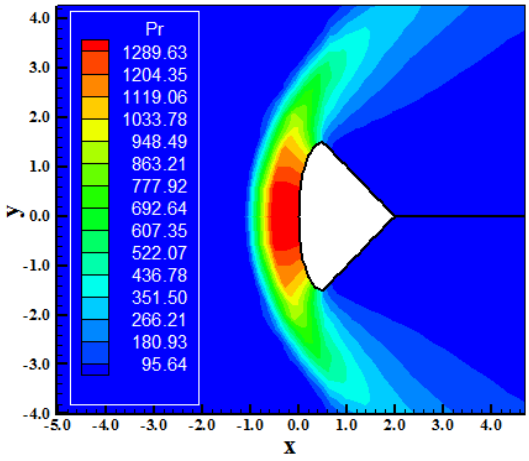

Figure 106. Pressure Contours (VL).

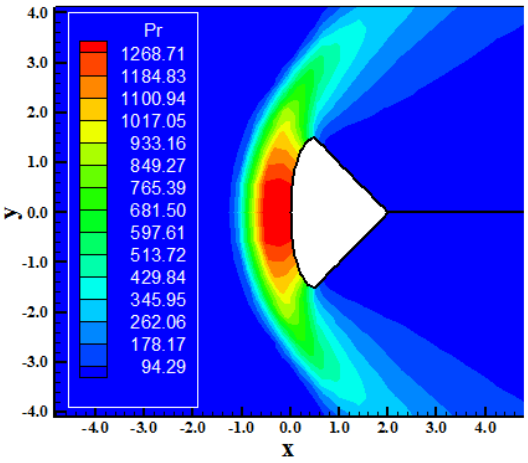

Figure 107. Pressure Contours (LS).

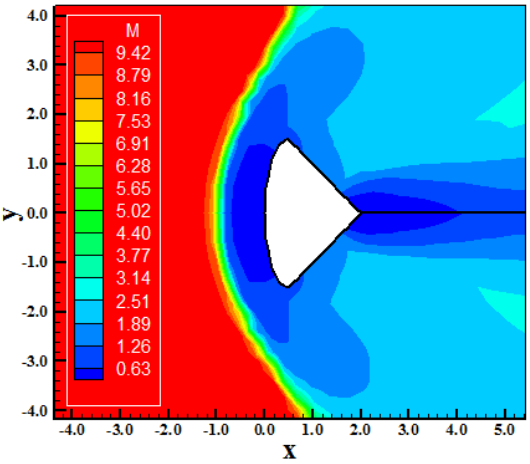

Figure 108. Mach Number Contours (VL).

Figures 106 and 107 show the pressure contours in the field obtained by the [6] and the [7] schemes, respectively. The most severe pressure field is obtained by the [6] scheme, characterizing this one as more conservative. Good symmetry properties are observed. The bow shock wave is well captured.

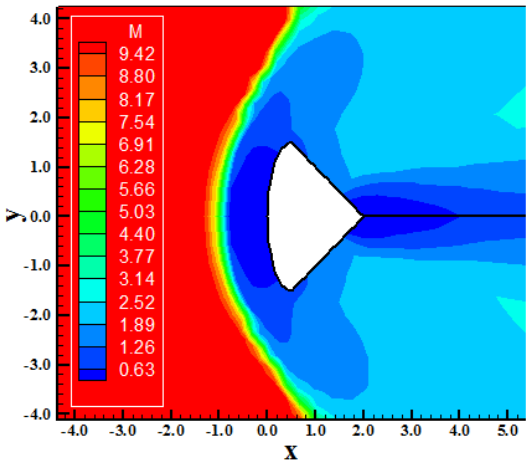

Figure 109. Mach Number Contours (LS).

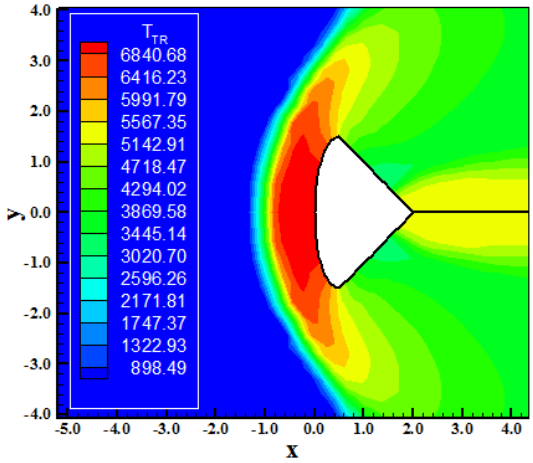

Figure 110. T/R Temperature Contours (VL).

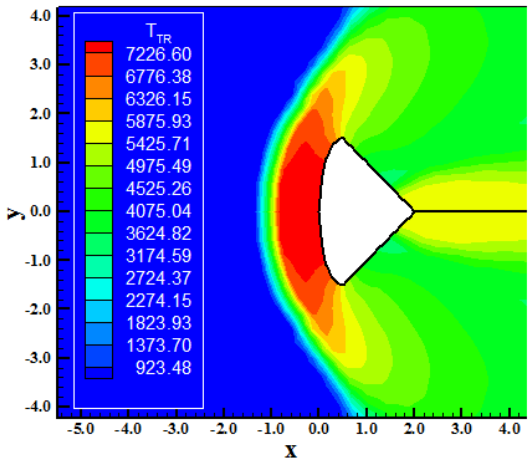

Figure 111. T/R Temperature Contours (LS).

Figures 108 and 109 presents the Mach number field generated by the [6] and by the [7] numerical algorithms, respectively. The most intense Mach number field is obtained by the [7] scheme. Good symmetry properties are observed. Figures 110 and 111 exhibit the translational / rotational temperature contours generated by the [6] and the [7] schemes, respectively. The most intense temperature field is obtained by the [7] scheme, as also the temperature peak of the order of 7,227 K. This temperature peak assures good N_2 and O_2 dissociations.

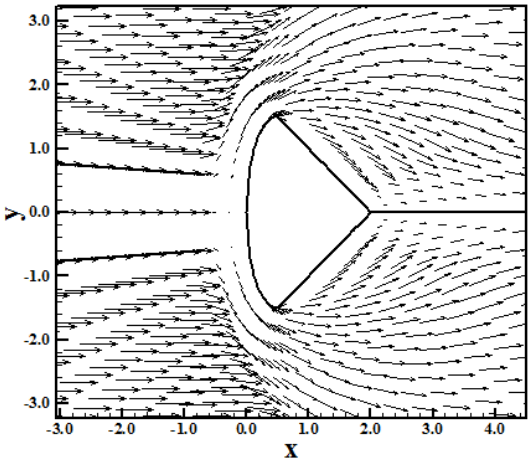

Figure 112. Velocity Vector Field (VL).

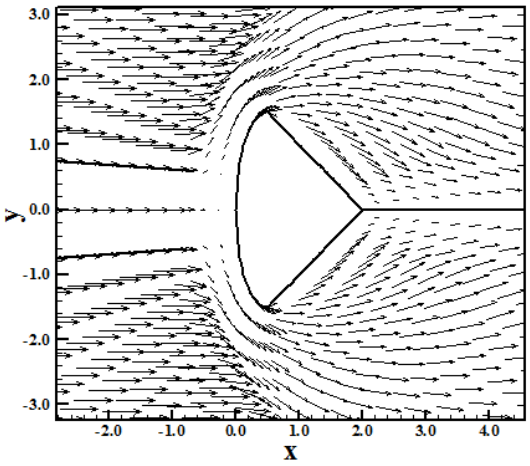

Figure 113. Velocity Vector Field (LS).

Figures 112 and 113 show the velocity vector field obtained by the [6] and the [7] algorithms, respectively. Good symmetry properties are observed. Moreover, the tangency and impermeability conditions are well satisfied by both schemes. The Kutta condition (flow at the trailing edge be continuous) is plenty satisfied. Figures 114 and 115 present the mass fraction distributions obtained by the [6] and the [7] algorithms, respectively. The N and O have good formations due to the good N_2 and O_2 dissociations. The NO has a reasonable formation due to the constancy in N_2 and O_2 dissociations, and in the N and O formations.

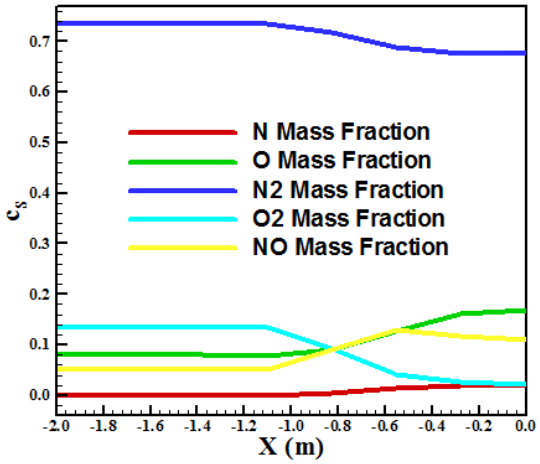

Figure 114. Mass fraction distributions at the stagnation line (VL).

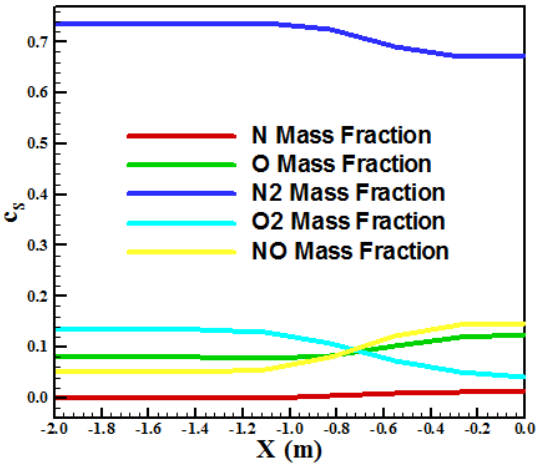

Figure 115. Mass fraction distributions at the stagnation line (LS).

3.4.4. Viscous, structured and second-order accurate case

Figures 116 and 117 show the pressure contours obtained by the [6] and the [7] numerical algorithms, respectively. The pressure fields are the same as in qualitative aspects as in quantitative aspects. Figures 118 and 119 present the Mach number fields generated by the [6] and the [7] algorithms, respectively. Good symmetry properties are observed as also the subsonic region behind the shock wave and the wave close to the trailing edge. Both schemes present the same Mach number field, without meaningful differences. Figures 120 and 121 present the translational / rotational temperature

contours generated by the [6] and the [7] schemes. The same temperature field is observed by both solutions, with a temperature peak of about 7,597 K, which yields good dissociation of N_2 and O_2. The temperature contours are the same in quantitative and in qualitative aspects.

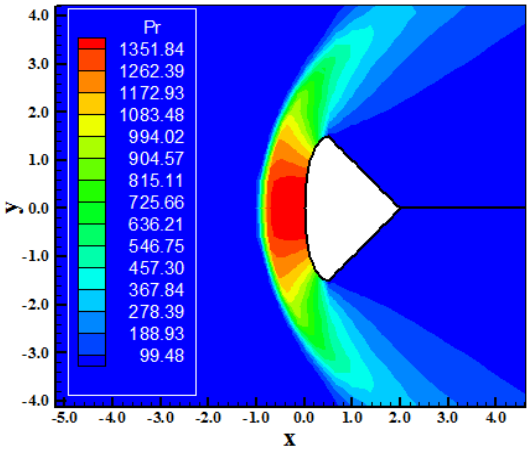

Figure 116. Pressure Contours (VL).

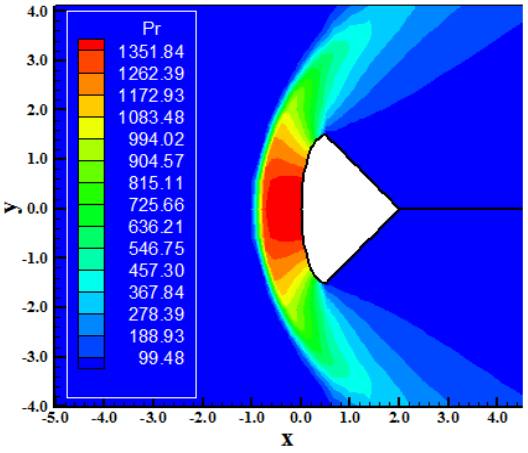

Figure 117. Pressure Contours (LS).

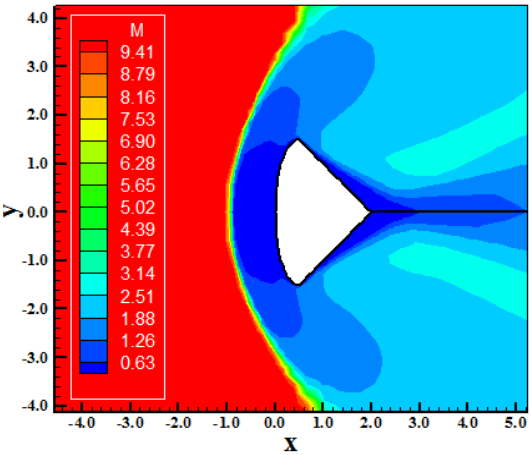

Figure 118. Mach Number Contours (VL).

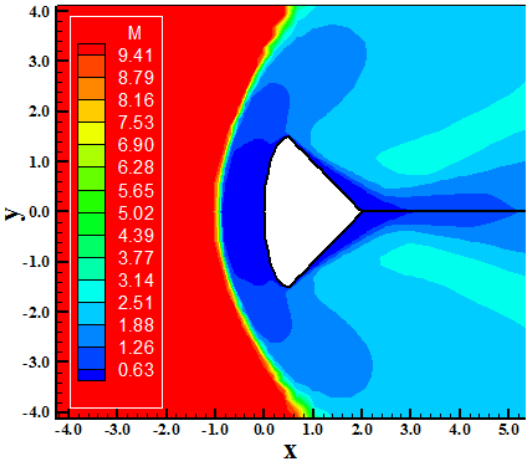

Figure 119. Mach Number Contours (LS).

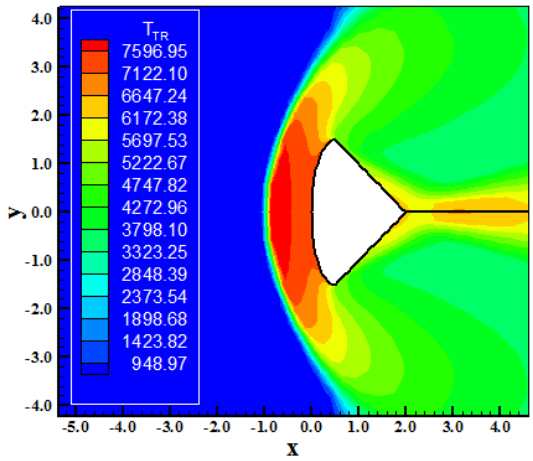

Figure 120. T/R Temperature Contours (VL).

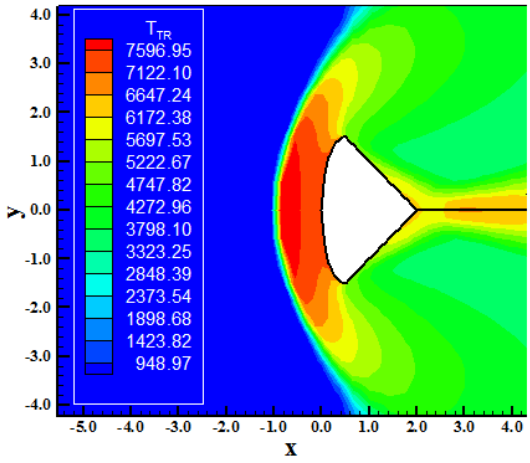

Figure 121. T/R Temperature Contours (LS).

Figures 122 and 123 present the velocity vector field obtained by the [6] and the [7] numerical schemes, respectively. Both solutions present the same characteristics, involving the capture of the

bow shock wave, satisfaction of the adherence and impermeability conditions, and symmetry properties. Both solutions capture the circulation bubbles formed at the trailing edge due to boundary layer separation.

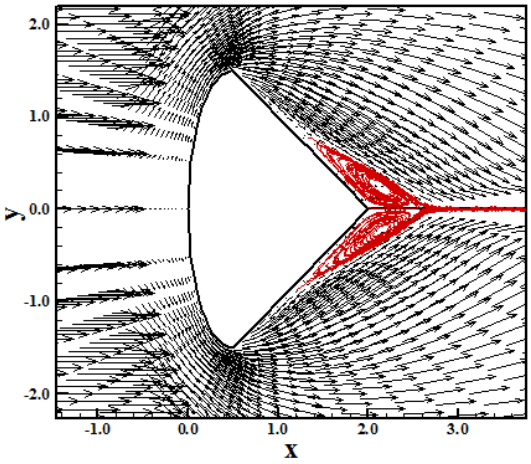

Figure 122. Velocity Vector Field (VL).

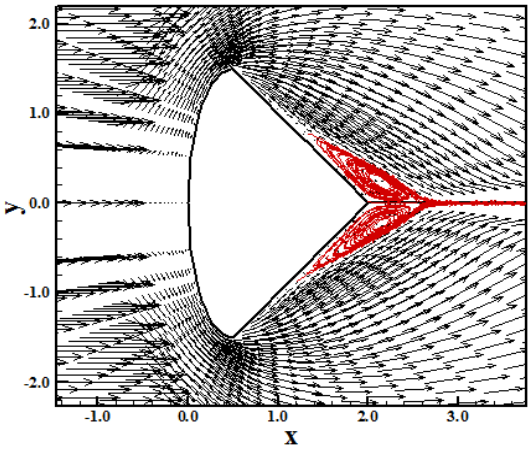

Figure 123. Velocity Vector Field (LS).

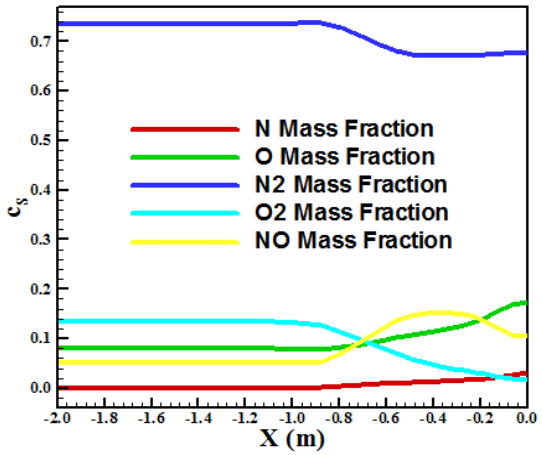

Figure 124. Mass fraction distributions at the stagnation line (VL).

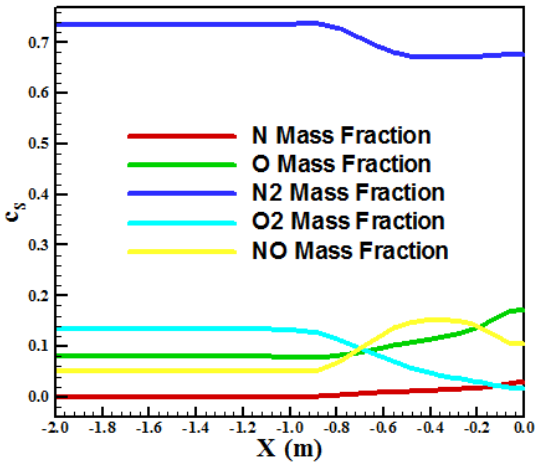

Figure 125. Mass fraction distributions at the stagnation line (LS).

Figures 124 and 125 exhibit the mass fraction distributions along the stagnation line of the re-entry capsule configuration, generated by the [6-7] schemes, respectively. Both solutions show the same mass fraction distributions with good formation of N and O and reasonable formation of the NO. The dissociations of N_2 and O_2 are very perceptible and contribute significantly by the aforementioned species.

4.3.5 Aerodynamic coefficients of lift and drag

Table 5 exhibits the aerodynamic coefficients of lift and drag obtained by the problem of the re-entry capsule, with structured discretization, to the reactive formulation. These coefficients are due to the pressure term alone. The contribution of the friction term was not considered.

Table 5. Aerodynamic coefficients of lift and drag to the structured re-entry case.

	[6] scheme		[7] scheme	
Case	c_L	c_D	c_L	c_D
$1^{st} - I^{(1)}$	4.134×10^{-10}	3.986	4.134×10^{-10}	3.986
$1^{st} - V^{(2)}$	-1.766×10^{-10}	4.378	-1.794×10^{-10}	4.378
$2^{nd} - I$	2.615×10^{-9}	4.077	2.030×10^{-9}	3.960
$2^{nd} - V$	-4.105×10^{-10}	4.311	-4.105×10^{-10}	4.311

(1): Inviscid; (2): Viscous.

To the problem of the re-entry capsule, a symmetric geometry in relation to the x axis, a zero value, or close to it, to the lift coefficient is expected. By Table 5, it is possible to note that the solution closest to this value to c_L was that of the [6] scheme with first-order accuracy, in an viscous

formulation. The maximum c_D was obtained by the solution of the [6] and the [7] schemes, first-order accurate and employing a viscous formulation.

4.4 Computational performance of the studied algorithms

Table 6 presents the computational data of the reactive simulations performed with the [6] and the [7] schemes to the problem of the blunt body, of the double ellipse, and of the re-entry capsule in two-dimensions. In this table are exhibited the studied case, the maximum number of CFL employed in the simulation, and the number of iterations to convergence.

Table 6. Computational data of the reactive simulations.

		[6] scheme		[7] scheme	
P[(1)]	Case	CFL	Iter	CFL	Iter
BB[(2)]	1st – I (SS)	0.3	1,304	0.6	529
	1st – V (SS)	0.1	8,069	0.6	1,381
	1st – I (AS)	0.3	1,224	0.3	1,064
	1st – V (AS)	0.2	5,753	0.2	7,150
DE[(3)]	1st – I	0.3	851	0.3	851
	1st – V	0.3	2,041	0.3	2,041
	2nd – I	0.3	711	0.3	711
	2nd – V	0.3	2,397	0.3	2,397
	1st – I (SS)	0.2	2,221	-	-
	1st – V (SS)	0.1	6,570	-	-
	1st – I (AS)	0.2	2,385	-	-
	1st – V (AS)	-	-	-	-
RC[(4)]	1st – I	0.4	1,050	0.4	1,050
	1st – V	0.1	7,805	0.1	7,805
	2nd – I	0.4	880	0.1	3,496
	2nd – V	0.1	4,879	0.1	4,879

[(1)]: Problem; [(2)]: Blunt Body; [(3)]: Double Ellipse; [(4)]: Reentry Capsule.

As can be observed, all test-cases converged with no minimal four orders of reduction in the value of the maximum residual. The maximum numbers of CFL presented the following distribution: 0.6 in two (2) cases (7.41%), 0.4 in three (3) cases (11.11%), 0.3 in eleven (11) cases (40.74%), 0.2 in four (4) cases (14.81%), and 0.1 in seven (7) cases (25.93%). The convergence iterations did not overtake 8,070, in all studied cases. However, the time wasted in the simulations was much raised, taking until weeks to convergence (to four orders of reduction in the maximum residual and viscous case). Finally, it is important to emphasize that all two-dimensional viscous simulations were considered laminar, although high Reynolds number were employed in the simulations.

5 Conclusions

This work, the second and last part of this study, presents two numerical tools implemented to simulate inviscid and viscous flows employing the reactive gas formulation of thermal equilibrium and chemical non-equilibrium flow in two-dimensions. The Euler and Navier-Stokes equations, employing a finite volume formulation, on the context of structured and unstructured spatial discretizations, are solved. These variants allow an effective comparison between the two types of spatial discretization aiming verify their potentialities: solution quality, convergence speed, computational cost, etc. The aerospace problems involving the "hot gas" hypersonic flows around a blunt body (unstructured), around a double ellipse (unstructured and structured), and around a re-entry capsule (structured), in two-dimensions, are simulated.

In the first paper of this work, it was presented the structured version of the calculation algorithms in two-dimensions and the [6] algorithm. In this paper, second part of this study, the unstructured formulation of the two-dimensional Euler and Navier-Stokes reactive equations and the [7] algorithm were presented.

The results have demonstrated that the most correct aerodynamic coefficient of lift is obtained by the [6] first-order accurate scheme in the viscous, structured, re-entry capsule simulation. Good dissociations of N_2 and O_2 were observed in all solutions, resulting in good formation of N, O and NO. The biggest mass fraction formation, resulting from the dissociations, in absolute terms, is due to the Oxygen. The Nitrogen had the biggest relative increase in relation to its original mass fraction value. The NO had a reasonable formation, due to the constancy in the O_2 and N_2 dissociations and the preferential formation of N and O.

In computational aspects, for the structured case, both algorithms presented good convergence speeds, as for instance, in the second-order version, double ellipse configuration and inviscid formulation (711 iterations). The most robust numerical scheme was the [6] scheme which simulated fifteen (15) cases, whereas the [7] scheme only simulated twelve (12) cases. The maximum number of CFL was obtained with the [7] scheme, on an unstructured context. The mesh alternated sense orientation resulted in good results, with more symmetrical solutions in the blunt body case. Even in the double ellipse case, better solution quality was obtained.

References:

[1] G. Degrez, and E. Van Der Weide, Upwind Residual Distribution Schemes for Chemical Non-Equilibrium Flows, *AIAA Paper 99-3366*, 1999.

[2] M. Liu, and M. Vinokur, Upwind Algorithms for General Thermo-Chemical Nonequilibrium Flows, *AIAA Paper 89-0201*, 1989.

[3] E. S. G. Maciel, and A. P. Pimenta, Chemical Non-Equilibrium Reentry Flows in Two-Dimensions – Part I, *submitted to WSEAS Transactions on Computers (to be published).*

[4] E. S. G. Maciel, Analysis of Convergence Acceleration Techniques Used in Unstructured Algorithms in the Solution of Aeronautical Problems – Part I, *Proceedings of the XVIII International Congress of Mechanical Engineering (XVIII COBEM)*, Ouro Preto, MG, Brazil, 2005. [CD-ROM]

[5] E. S. G. Maciel, Analysis of Convergence Acceleration Techniques Used in Unstructured Algorithms in the Solution of Aerospace Problems – Part II, *Proceedings of the XII Brazilian Congress of Thermal Engineering and Sciences (XII ENCIT)*, Belo Horizonte, MG, Brazil, 2008. [CD-ROM]

[6] B. Van Leer, Flux-Vector Splitting for the Euler Equations, *Lecture Notes in Physics*, Springer Verlag, Berlin, Vol. 170, 1982, pp. 507-512.

[7] M. Liou, and C. J. Steffen Jr., A New Flux Splitting Scheme, *Journal of Computational Physics*, Vol. 107, 1993, pp. 23-39.

[8] R. Radespiel, and N. Kroll, Accurate Flux Vector Splitting for Shocks and Shear Layers, *Journal of Computational Physics*, Vol. 121, 1995, pp. 66-78.

[9] L. N. Long, M. M. S. Khan, and H. T. Sharp, Massively Parallel Three-Dimensional Euler / Navier-Stokes Method, *AIAA Journal*, Vol. 29, No. 5, 1991, pp. 657-666.

[10] R. W. Fox, and A. T. McDonald, *Introdução à Mecânica dos Fluidos*, Guanabara, 1988.

[11] E. S. G. Maciel, Relatório ao CNPq (Conselho Nacional de Desenvolvimento Científico e Tecnológico) sobre as atividades de pesquisa realizadas no período de 01/07/2008 até 30/06/2009 com relação ao projeto PDJ número 150143/2008-7, *Technical Report, National Council of Scientific and Technological Development (CNPq)*, São José dos Campos, SP, Brasil, 102p, 2009.

[12] E. S. G. Maciel, and A. P. Pimenta, Thermochemical Non-Equilibrium Reentry Flows in Two-Dimensions – Part II, *WSEAS Transactions on Mathematics*, Vol. 11, Issue 11, November, 2012, pp. 977-1005.